Pyruvate dehydrogenase deficiency hijacks B12 to sustain energy production

Duo Duan[1,2,3], Chunxia Qin [1,2,3], Jie Chen[1,2,3], Shiyu Liu[4,5], Shihao Zhu[1,2,3], Zicheng Liu[1,2,3], Hai-Lin Dong[6,7], Bingbing Wu[8], Ting Zhang[9], Zhi-Ying Wu[6,7]*, Shengnan Wu[10]*, Wei Lu[11]*, Xinwen Huang[9]*, Lianfeng Wu[1,2,3]*

[1]School of Life Sciences, Westlake University, Hangzhou, Zhejiang, China.

[2]Westlake Laboratory of Life Sciences and Biomedicine, Hangzhou, Zhejiang, China.

[3]Institute of Basic Medical Sciences, Westlake Institute for Advanced Study, Hangzhou, Zhejiang, China.

[4]School of Basic Medical Sciences, Capital Medical University, Beijing, China.

[5]Institute for Medical Physiology, Chinese Institutes for Medical Research (CIMR), Beijing, China.

[6]Department of Medical Genetics and Center for Rare Diseases, Second Affiliated Hospital, Zhejiang University School of Medicine, and Zhejiang Key Laboratory of Rare Diseases for Precision Medicine and Clinical Translation, Hangzhou, China.

[7]Nanhu Brain-computer Interface Institute, Hangzhou, China.

[8]Center for Molecular Medicine, Children's Hospital of Fudan University, National Children's Medical Center, Shanghai 201102, China.

[9]Department of Genetics and Metabolism，Children's Hospital, Zhejiang University School of Medicine, National Clinical Research Center for Children and Adolescents' Health and Diseases.

[10]Department of Clinical Laboratory, Shanghai Children's Hospital, School of Medicine, Shanghai Jiao Tong University, Shanghai, China

[11]Department of Endocrinology and Metabolism, Children's Hospital of Fudan University, National Children's Medical Center, Shanghai 201102, China

Abstract

The pyruvate dehydrogenase complex (PDC) serves as the crucial gate between cytosolic and mitochondrial metabolism[1]. In humans, PDC deficiency (PDCD) leads to a severe mitochondrial disorder without effective treatment[2,3,4]. Beyond its known enzymatic defect, the broader metabolic consequences of PDCD remain unclear. Using cross-species approaches spanning *Caenorhabditis elegans*, mouse primary hepatocytes, human cell lines, and patient blood samples, we reveal a conserved and obligatory metabolic trade-off in PDCD: functional depletion of vitamin B12. This loss is driven by compensatory rewiring via an MDT-15/MED15-NHR-68/HNF4 pathway, diverting carbon flux from B12-dependent propionate metabolism to sustain acetyl-CoA synthesis and mitochondrial function. Thus, PDCD triggers an acquired B12 deficiency as a survival strategy. Therapeutically, this vulnerability is targetable, as acetate supplementation restores acetyl-CoA levels and rescues B12 function. Our work reveals a fundamental adaptive principle where a vital vitamin-dependent pathway is sacrificed to maintain core energy production, unveiling novel therapeutic avenues.

Main

The pyruvate dehydrogenase complex (PDC) catalyzes the irreversible oxidation of pyruvate to acetyl-CoA, serving as a critical metabolic gatekeeper between cytosolic glycolysis and central mitochondrial metabolism, including tricarboxylic acid (TCA) cycle and oxidative phosphorylation[1]. PDC deficiency (PDCD) is a devastating inborn error of metabolism (IEM), characterized by systemic energy deficits, lactic acidosis, and profound neurodevelopmental impairment[2,3]. Although considered rare[5], PDCD is a significant cause of severe, often fatal, childhood neurometabolic disease[4]. While the primary enzymatic defect, impaired acetyl-CoA generation from glycolytic pyruvate, is well-defined, the full scope of consequent systemic metabolic adaptations and their contribution to pathophysiology remains unclear, hindering the development of effective therapies.

Animal models of PDCD, including constitutive and tissue-specific murine knockouts[6,7,8,9] as well as zebrafish mutants[10], have been instrumental in recapitulating key pathological features such as lactic acidosis, neurological dysfunction, and embryonic lethality. These studies have confirmed the central energy crisis and established the critical role of the PDC in fueling the TCA cycle. However, they have also revealed surprising metabolic flexibility and organ-specific adaptations[7,9], hinting at the activation of uncharacterized compensatory networks that may involve the rerouting or sacrifice of other essential metabolic pathways to support survival.

Vitamin B12 (B12, cobalamin) is a pivotal cofactor in one-carbon and mitochondrial shot chain fatty acid metabolism. It serves as an essential coenzyme for two crucial enzymes: methyl malonyl-CoA mutase (MUT), required for propionate metabolism and odd-chain fatty acid oxidation, and methionine synthase (MTR), which is vital for methylation cycles and homocysteine

remethylation[11,12]. Functional B12 status is therefore accurately reflected not solely by its serum levels but by the accumulation of its substrates: elevated methylmalonic acid (MMA) and homocysteine (HCY), which are established biomarkers of intracellular B12 deficiency[13]. Intriguingly, the occurrence of "functional" B12 deficiency has been recognized in clinic, where MMA and HCY are elevated despite normal serum B12 levels, indicating impaired cellular utilization of the vitamin independent of its availability[14]. Disruption of B12-dependent processes, either through functional inhibition or decreased B12 levels, results in severe neurological and metabolic impairments[11]. Nevertheless, a direct association between B12 function and PDC activity has not yet been established.

The nematode *Caenorhabditis elegans* (*C. elegans*) offers a powerful model for metabolic research due to its genetic tractability, evolutionarily conserved metabolic pathways, and physiological transparency, enabling *in vivo* analysis of cellular metabolic responses[15,16,17,18,19]. In this study, we employ a cross-species approach integrating *C. elegans*, mouse hepatocytes, human cell lines and patients' blood samples to investigate the systemic metabolic consequences of PDCD. Using a newly established *C. elegans* model of PDCD, we uncover a profound and unexpected impairment in B12 function. This defect is conserved in mammalian PDCD models, indicating a fundamental metabolic principle. We demonstrate that PDCD initiates a transcriptional rewiring program, mediated by a conserved MDT-15/MED15–NHR-68/HNF4 axis, which shunts metabolism toward B12-independent propionate flux and one-carbon metabolism. Crucially, we reveal that this rewiring constitutes a strategic trade-off: the ablation of canonical B12 function is necessary to redirect carbon toward acetyl-CoA synthesis, thereby sustaining TCA cycle anaplerosis and energy production. This survival-oriented metabolic compromise creates a metabolically vulnerable state, which we find can be therapeutically targeted, as acetate supplementation bypasses the deficit,

restores acetyl-CoA pools, and rescues B12 function. Our findings elucidate a conserved adaptive metabolic strategy in PDCD, in which the sacrifice of one vital vitamin-dependent pathway becomes indispensable to sustain core energy production, uncovering new potential therapeutic options.

Establishment of a *C. elegans* model for PDCD

PDC is a critical mitochondrial gateway, catalyzing the conversion of pyruvate into acetyl-CoA to fuel the tricarboxylic acid (TCA) cycle for energy production (Fig. 1a). This multi-enzyme complex comprises three core components: the E1 subunit (pyruvate dehydrogenase), which decarboxylates pyruvate; the E2 subunit (dihydrolipoamide acetyltransferase), which transfers an acetyl group to coenzyme A; and the E3 subunit (dihydrolipoamide dehydrogenase), which regenerates the oxidized lipoamide cofactor[20].

During a routine mutagenesis screen using *C. elegans*, we came across a PDC mutant carrying a point mutation (A111V) in a conserved residue of PDHA-1, which is the E1α subunit of PDC (Fig. 1b and 1c). This mutation significantly reduced PDC enzymatic activity to approximately 35% of wild-type (WT) levels (Fig. 1d), a deficiency comparable to that observed in PDCD patients[21]. Consistent with human PDCD pathology[22], the *pdha-1*^{A111V} mutant exhibited a nearly two-fold increase in lactate accumulation (Fig. 1e). Isotopic tracing with ^{13}C-glucose confirmed PDC as a critical metabolic node, revealing an accumulation of glycolytic intermediates and a severe impairment of carbon flux into the TCA cycle (Fig. 1f, g). These central metabolic disruptions were replicated following *pdha-1* RNAi knockdown (Extended Data Fig. 1a-f), confirming that the observed phenotypes are a direct consequence of *pdha-1* deficiency. The mutant animals also displayed pronounced physiological deficits, including developmental delay, severely impaired

113 motility, and a reduced brood size (Fig. 1h-1k), phenotypes that recapitulate key aspects of human
114 PDCD[2]. Collectively, these data demonstrate that the *pdha-1*^{A111V} mutant recapitulates the
115 hallmark metabolic and physiological features of human PDCD, establishing it as a powerful
116 model system for elucidating the comprehensive pathological spectrum of this disorder.
117
118 **PDCD induces an evolutionarily conserved B12 dysfunction**
119 To define the transcriptional consequences of PDCD, we carried out RNA sequencing (RNA-seq)
120 analysis following *pdha-1* knockdown. This analysis revealed a signature of severe neurological
121 dysfunction, including upregulation of neuropeptide signaling genes and broad downregulation of
122 nucleic acid metabolism genes (Extended Data Fig. 2a, b), consistent with clinical manifestations
123 in PDCD patients[2]. Strikingly, we also observed a coordinated upregulation of genes involved in
124 amino acid catabolism, particularly those comprising the propionate shunt pathway (Fig. 2a-2c
125 and Extended Data Fig. 2a). In *C. elegans*, induction of this pathway, specifically the key enzyme
126 encoded by *acdh-1*, serves as a sensitive transcriptional biomarker for functional B12
127 deficiency[23,24,25]. Genetic disruption of PDC, achieved through mutation or RNAi-mediated
128 knockdown of *pdha-1* or other core PDC subunits, robustly induced *acdh-1* expression (Fig. 2d
129 and Extended Data Fig. 2c), confirming that PDC disruption triggers this B12 deficiency signature.
130 As *acdh-1* is mainly expressed in the intestine, we restored *pdha-1* expression specifically in this
131 tissue within the *pdha-1*^{A111V} mutant background (Extended Data Fig. 2d). This tissue-specific
132 restoration was sufficient to restore the B12 activity in mediating *acdh-1* expression (Extended
133 Data Fig. 2e), suggesting that PDC regulates B12 function in a cell-autonomous manner.
134
135 We next asked whether PDCD globally impairs the organism's response to B12 treatment.
136 Principal component analysis (PCA) of transcriptomes from animals treated with *pdha-1* RNAi ±

B12 revealed that the distinct transcriptional shift driven by B12 supplementation in controls was virtually abolished under PDC-deficient conditions (Fig. 2e). Specifically, the normal B12-mediated repression of propionate shunt genes (*acdh-1, ech-6, hach-1, hphd-1, alh-8*), downregulation of B12 transport/processing genes (*pmp-5, cblc-1, mtrr-1, mmab-1*) and methionine cycle regulators (*msra-1, metr-1, ahcy-1*) were significantly attenuated (Fig. 2f). qPCR analysis confirmed a complete failure of B12 to repress the propionate shunt pathway in PDC-deficient animals (Fig. 2g). We then tested if this transcriptional blockade translated to functional B12 resistance. Consistent with the RNA-seq data, canonical B12-dependent phenotypes were abolished by PDCD: 1) the B12-mediated acceleration of development, linked to methionine cycle activation[26,27], was almost entirely abrogated (Fig. 2h), and 2) the protective effect of B12 against toxicity from propionate shunt metabolites, via enhanced mitochondrial fatty acid β-oxidation[23] was completely lost, as shown by survival assays following *hach-1* RNAi (Fig. 2i).

To determine if PDCD alters functional B12 availability, we measured B12 levels and downstream metabolic markers via mass spectrometry. While the results revealed unchanged levels of active B12 forms (Fig. 2j, k) and MMA (Extended Data Fig. 2f), a canonical B12 status marker[28], we observed a significant HCY increase (Fig. 2l). HCY is a sensitive functional marker of impaired B12-dependent methionine synthesis[28,29], indicating a potential compartmentalized or functional B12 deficiency despite its normal systemic levels. To eliminate confounding bacterial metabolism, we utilized a chemically defined, axenic culture medium (*C. elegans* Habituation and Reproduction media, CeHR)[15,30]. In this system, B12 deprivation potently induced *acdh-1* in WT animals (Fig. 2m). In stark contrast, the *pdha-1*^{A111V} mutant was completely resistant to B12, with even 10 μM B12 failing to repress *acdh-1* expression (Fig. 2m). Furthermore, supplementation with either bioactive form of B12 (adenosyl-cobalamin, Ado-B12 or methyl-cobalamin, Met-12)

was ineffective (Fig. 2m), ruling out defects in B12 processing or activation as the primary cause of B12 dysfunction in PDCD.

C. elegans possesses two genes, *mmcm-1* and *metr-1*, which encode the B12-dependent enzymes, MUT and MTR, respectively[12]. The *pdha-1* mutation elevated *acdh-1* expression to a level exceeding that caused by knockdown of either *mmcm-1* or *metr-1* alone, and comparable to that of *mmcm-1; metr-1* double mutants (Extended Data Fig. 2g, h). Critically, neither depleting *mmcm-1* or *metr-1* in the *pdha-1*^{A111V} mutant, nor knocking down *pdha-1* in the *mmcm-1; metr-1* double mutant background, further increased *acdh-1* expression (Extended Data Fig. 2g, h). This genetic epistasis demonstrates that PDC deficiency functionally disrupts both major branches of B12-dependent metabolism. Collectively, our data from transcriptional profiling, functional phenotyping, metabolite analysis, and genetic interaction studies reveal that PDCD induces a state of functional B12 deficiency in *C. elegans*, independent of B12 availability.

To evaluate the conservation of PDC's role in B12-dependent metabolism, we first validated the responsiveness of the propionate shunt pathway in mouse primary hepatocytes, where its homologous genes express[23]. Consistent with worm models, supplementation with propionate dose-dependently induced the expression of propionate shunt genes (Extended Data Fig. 3). Inhibiting PDC with 3-fluoropyruvate (3-FP), a competitive PDHA1 antagonist[31], recapitulated key features of functional B12 deficiency in mouse cells, as it significantly upregulated propionate shunt genes (Fig. 3a, b) and increased HCY levels in mouse primary hepatocytes (Fig. 3c). We next examined the conservation of this interaction in a human cellular context. Because certain cancers utilize B12 to recycle HCY into methionine for survival under methionine restriction[32], we tested the human hepatocellular carcinoma line Huh7. While these cells proliferated in

methionine-free medium supplemented with HCY, co-treatment with a PDC inhibitor effectively blocked this rescue (Fig. 3d), demonstrating a requirement for PDC activity in sustaining B12-dependent methionine synthesis in human cells. Finally, we analyzed blood samples from patients with genetically confirmed PDCD (Supplementary Table 1). As anticipated, elevated lactate confirmed systemic PDC dysfunction (Fig. 3e). Crucially, despite relatively normal blood B12 levels, these patients exhibited significantly elevated MMA (Fig. 3f, g). This provides direct clinical evidence that impaired PDC activity leads to a functional B12 deficiency. Together, these results from mouse hepatocytes, human cancer cells, and patient samples establish the conservation of a fundamental regulatory axis in which PDC function is required for normal B12 metabolism, from invertebrates to humans.

PDCD impairs B12 function by activating the MDT-15–NHR-68–dependent propionate shunt

To elucidate the mechanism of PDCD-induced B12 dysfunction, we conducted an ethyl methanesulfonate (EMS) suppressor screen in the *pdha-1*^{A111V} mutants (Fig. 4a). Strikingly, we discovered 20 independent mutants mapping to two nuclear hormone receptors (NHR), *nhr-68* (19 mutants) and *nhr-10* (1 mutant) and one mutant in the Mediator gene *mdt-15* (Fig. 4a). Disruption of *nhr-68*, *nhr-10*, or *mdt-15* by mutation or RNAi strongly suppressed *acdh-1* induction in the *pdha-1*^{A111V} background (Fig. 4b and Extended Data Fig. 4a). Furthermore, *nhr-68* knockdown broadly attenuated induction of the entire shunt pathway regulon (Fig. 4c). NHR-68 and NHR-10 were recently reported to function as an AND-logic gate[24] (Fig. 4d). Supporting this model, a *nhr-10*^{P264S} gain-of-function (*gof*) mutant, which exhibited constitutive nuclear NHR-10 localization, dominantly activated *acdh-1* expression (Fig. 4e and Extended Data Fig. 4b). This *nhr-10*^{P264S} *gof* mutation promoted nuclear accumulation of NHR-68 (Fig. 4f, g), and *nhr-68* knockdown

suppressed the resulting *acdh-1* induction (Fig. 4h), confirming the essential role of NHR-68 in the AND-logic gate. Notably, the *nhr-10* ^{P264S} *gof* mutation alone recapitulated the hallmark phenotypes of B12 impairment, elevated HCY levels and blocked B12-dependent developmental acceleration (Fig. 4i, j), indicating that propionate shunt pathway activation is sufficient to inhibit B12 function.

MDT-15 is a known partner of NHR-68 and NHR-10 in regulating propionate shunt gene expression[33]. To define their roles in PDCD signaling, we examined their genetic epistasis by monitoring NHR-68 localization. PDCD markedly induced NHR-68 nuclear accumulation (Fig. 4k, l). Intriguingly, RNAi knockdown of *mdt-15*, but not *nhr-10*, blocked this accumulation in the *pdha-1*^{A111V} mutants (Fig. 4k, l), placing MDT-15 upstream of NHR-68. This also suggests that NHR-10 converges on the pre-existing AND-logic gate, where NHR-68 transduces the PDCD signal. Critically, loss of *nhr-68* nearly completely recued PDCD-induced B12 dysfunction: the *nhr-68*^{Q47*} mutation significantly lowered HCY levels and restored the B12-dependent development acceleration in the *pdha-1*^{A111V} animals (Fig. 4m, n). In a consistent manner, depleting *acdh-1* also recovered B12's developmental benefit (Extended Data Fig. 4c). Collectively, our data establish that PDCD impairs B12 function by activating the propionate shunt pathway via an MDT-15–NHR-68 signaling axis (Fig. 4o).

PDCD-induced B12 dysfunction results from and benefits propionate shunt activation to fuel acetyl-CoA

Propionate shunt activation is typically viewed as a consequence of B12 deficiency [23]. To investigate how it actively suppresses B12 function in PDCD, we knocked down individual shunt genes in *pdha-1*^{A111V} mutants (Fig. 5a). Strikingly, knockdown of *acdh-1*, but not *ech-6* or *hach-1*,

significantly attenuated HCY accumulation and restored B12-dependent development acceleration (Fig. 5b, c). Furthermore, depleting *acdh-1* exacerbated phenotypic severity in *pdha-1*^{A111V} mutants, causing more profound growth, fertility, and motility defects (Fig. 5d-5g). This demonstrates that ACDH-1 is essential for survival in PDCD and is responsible for the resultant B12 dysfunction.

ACDH-1 catalyzes the conversion of propionyl-CoA to acrylyl-CoA (Fig. 5a). We therefore hypothesized that its product, acrylyl-CoA, might directly inhibit B12 function, consistent with reports that other CoA metabolites can induce B12 deficiency[34,35,36]. Supporting this, treatment with acrylate, an analog of acrylyl-CoA, induced *acdh-1* expression, elevated HCY, and impaired B12-mediated developmental acceleration (Fig. 5h, i). These findings suggest that acrylyl-CoA accumulation from shunt activation directly disrupts B12-dependent metabolism in PDCD.

This cross-inhibition theoretically drives propionate metabolism to fuel acetyl-CoA. To test this, we utilized isotopic tracing combined with computational flux analysis[37] to monitor propionate metabolism in PDCD and WT animals. The analysis revealed marked metabolic rewiring in mutants: pyruvate flux into the TCA cycle via PDC was substantially reduced, with carbon diverted toward lactate, alanine, and oxaloacetate (Fig. 5j). Importantly, the canonical B12-dependent conversion of propionate to succinyl-CoA was significantly inhibited (Fig. 5j, k), confirming a block in B12 function. In contrast, PDCD mutants rerouted substantially more propionate through the shunt pathway than WT, despite unchanged propionate and propionyl-CoA levels (Fig. 5j, 5l, Extended Data Fig 5. a, b). This shunt activation supplied nearly 73% of the cellular acetyl-CoA pool (Fig. 5m and 5n), underscoring its essential role and the resultant B12 dysfunction, in maintaining metabolic homeostasis under PDC deficiency (Fig. 5o).

Acetate supplementation replenishes acetyl-CoA and restores B12 function in PDCD

Given the critical role of acetyl-CoA depletion in PDCD pathology, we asked whether this metabolic defect was targetable. We tested acetate administration, an established approach to boost cellular acetyl-CoA[38,39], in *pdha-1*^{A111V} mutants. Acetate markedly suppressed *acdh-1* expression in these mutants but not in *mmcm-1* mutants (Fig. 6a), indicating specificity for rescuing the acetyl-CoA deficit caused by PDC deficiency. Furthermore, acetate inhibited NHR-68 nuclear localization, reduced HCY accumulation, and restored B12-dependent developmental acceleration in *pdha-1*^{A111V} mutants (Fig. 6b-6e), confirming that acetyl-CoA depletion drives the metabolic rewiring in PDCD.

We next assessed the physiological impact of acetate under conditions of shunt pathway blockade. While inhibiting the propionate shunt in WT animals caused no overt defects, it severely exacerbated developmental delay, reduced body size, and impaired motility in *pdha-1*^{A111V} mutants (Fig. 6f-6g). Importantly, acetate supplementation significantly rescued these phenotypes in *pdha-1*^{A111V}*; nhr-68*^{Q47*} double mutants (Fig. 6f-6g), demonstrating acetyl-CoA depletion underlies their severity and reinforcing acetate's therapeutic potential.

Although total acetyl-CoA levels were maintained in *pdha-1*^{A111V} mutants alone, introducing the *nhr-68*^{Q47*} mutation to block the propionate shunt significantly reduced acetyl-CoA (Fig. 6h). This reduction was nearly fully rescued by acetate, underscoring the propionate shunt pathway's essential role in maintaining acetyl-CoA homeostasis. Consistent with this, Seahorse analysis revealed that *pdha-1*^{A111V} mutants maintained normal respiratory capacity, whereas the *nhr-68*^{Q47*} mutation substantially inhibited the basal oxygen consumption rate (OCR) in *pdha-1*^{A111V} mutants, an effect reversed by acetate (Fig. 6i, j). Taken together, we propose an adaptive metabolic

compensation mechanism: PDCD is sensed by a coordinated MDT-15–NHR-68/10 module, which reprograms propionate metabolism by activating the shunt pathway. This response sustains acetyl-CoA and viability but occurs at the cost of B12 function, representing a critical metabolic trade-off under PDC deficiency (Fig. 6k).

Discussion

PDCD provides a unique model to investigate how organisms adapt when a central energy-producing pathway is disrupted, as it fundamentally ruins the critical link between glycolysis and the TCA cycle[22]. Understanding these adaptations is crucial not only for elucidating pathogenesis but also for uncovering broader principles of metabolic resilience. Initiating the finding from a *C. elegans* model, we demonstrate that PDCD triggers an evolutionarily conserved metabolic adaptation in which the functional sacrifice of B12 becomes an obligatory strategy to sustain core energy production. Our work underscores a critical principle in metabolic homeostasis: during severe deficits in non-redundant, critical pathways such as pyruvate oxidation, survival necessitates extensive metabolic rewiring that can involve the active impairment of other vital processes. To the best of our knowledge, this is the first report showing that the deficiency of one essential metabolic mechanism can actively undermine another as an adaptive survival strategy. Collectively, this work not only uncovers a targetable vulnerability in PDCD but also reinforces the utility of *C. elegans* as a fundamental discovery platform[40], particularly for metabolic and IEM research.

Our data demonstrate that the functional link between PDC activity and B12 function is a shared metabolic principle across species. B12 has long been recognized as essential for propionate catabolism and one-carbon metabolism in metazoans, and its functional deficiency leads to

conserved biochemical signatures[11,41]. Notably, phylogenomic analyses indicate that although B12 is indispensable for animals, many other eukaryotes employ B12-independent enzymes[42,43], suggesting an evolutionary plasticity in the choice of metabolic routes. Together with previous findings[14,23], our study demonstrates that the physiological relevance of an essential vitamin is not determined solely by its availability but is dynamically modulated by the broader metabolic network of the organism.

Our findings reveal that in PDCD, the organism proactively initiates a transcriptional program to reroute propionate metabolism, rather than merely enduring a passive depletion of acetyl-CoA. This program is likely initiated via the conserved metabolic integrator MDT-15/MED15[44,45] and executed by the nuclear receptors NHR-68/HNF4 and NHR-10/HNF4 to divert carbon flux toward a compensatory salvage pathway. We propose a model whereby the acetyl-CoA deficit is sensed, leading to MDT-15/MED15-dependent activation of the NHR-68/HNF4–NHR-10/HNF4 complex. Intriguingly, recent reports indicate cells possess mechanisms to sense acetyl-CoA levels and mediate mitochondrial homeostasis[46]. Whether NHR-68/HNF4 or MDT-15/MED15 directly senses this deficit remains to be determined.

In the current study, we posit acrylyl-CoA, generated in the propionate shunt pathway, as a potential endogenous inhibitor of B12-dependent enzymes. This is supported by our findings that supplementing acrylate metabolites replicates B12 function inhibition, and that genetically disrupting the shunt pathway severely exacerbates phenotypic deficits. While increases in other CoA metabolites, such as itaconyl-CoA[34,36] and malyl-CoA[35] have been linked to B12 activity loss, direct structural analysis of acrylyl-CoA complexed with B12-dependent enzymes will be necessary to validate this specific connection.

Clinically, despite the empirical use of a "mitochondrial treatment cocktail"[47], there remains a lack of approved therapies for PDCD[2]. Our demonstration that acetate supplementation alleviates metabolic and functional deficits in PDC deficiency suggests a promising therapeutic strategy aimed at restoring acetyl-CoA pools, rather than merely increasing B12 levels. This approach is supported by observations that systemic acetate administration reverses neuronal disorders in a brain-specific PDCD mouse model[6]. Therefore, future efforts are warranted to establish the efficacy, optimal dosing, and safety of acetate supplementation in PDCD management.

Materials and Methods

C. elegans culture methods and strains

General methods for worm culturing were performed as previously described[48]. All nematode strains were maintained at 20°C, grown on nematode growth medium (NGM) plates seeded with *E. coli* OP50-1. All experiments were conducted with synchronized *C. elegans* hermaphrodites fed on *E. coli* HT115, unless otherwise indicated. The *E. coli* strains OP50-1 and HT115 were obtained from the CGC. B12 deprivation on NGM plate was achieved by cultivating *E. coli* in B12-deficient LB medium, in which tryptone was replaced with neutralized soy-peptone, and accordingly by substituting tryptone with neutralized soy-peptone in NGM[12]. N2 Bristol was used as the WT strain.

The following strains have been used:

Genotype	**Source**	**Identifier**
N2 Bristol	CGC	N2
pdha-1^{A111V} *(aly3)*	This study	WLU130
wwIs24 [acdh-1p::GFP + unc-119(+)]	CGC	VL749

pdha-1^{A111V} (aly3); wwIs24 [acdh-1p::GFP + unc-119(+)]	This study	WLU129
pdha-1^{A111V} (aly3); nhr-68^{Q47*} (aly5); wwIs24 [acdh-1p::GFP+unc-119(+)]	This study	WLU381
nhr-68^{Q47*} (aly5)	This study	WLU384
pdha-1^{A111V} (aly3); nhr-68^{Q47*} (aly5)	This study	WLU382
pdha-1^{A111V} (aly3); nhr-10^{R43C} (aly60); wwIs24 [acdh-1p::GFP+unc-119(+)]	This study	WLU632
pdha-1^{A111V} (aly3); mdt-15^{P704L} (aly91); wwIs24 [acdh-1p::GFP+unc-119(+)]	This study	WLU711
alyIs15[Pnhr-68::nhr-68::RFP; Pmyo-2::RFP]	This study	WLU466
pdha-1^{A111V} (aly3); alyIs15[Pnhr-68::nhr-68::RFP; Pmyo-2::RFP]	This study	WLU465
nhr-10^{P264S} (aly92); wwIs24 [acdh-1p::GFP+unc-119(+)]	This study	WLU63
alyIs20[Pnhr-10::nhr-10::RFP; Pmyo-2::GFP]	This study	WLU220
alyEx117[nhr-10p::nhr-10^{P264S}::RFP+myo-2p::GFP]	This study	WLU725 (L1 arrest)
metr-1 (ok521); mmcm-1 (ok163); wwIs24 [acdh-1p::GFP + unc-119(+)]	This study	WLU236
mmcm-1(ok1637) III; wwIs24 [acdh-1p::GFP + unc-119(+)].	This study	WLU183
alyIs55 [ges-1p::pdha-1::GFP]	This study	WLU388
acdh-1 (ok1489)	CGC	VC1011
acdh-1 (ok1489); pdha-1^{A111V} (aly3)	This study	WLU604

Axenic medium culture

The CeHR medium was prepared following a previously described protocol[15,49]. B12-deficient CeHR was prepared without the supplementation of B12. Synchronized L1 worms were cultured in CeHR medium with continuous shaking at 70 rpm on a shaker at 20 °C. Synchronization was conducted according to the hypochlorite method to remove bacteria.

Chemicals

Cyanocobalamin (CN-B12, Sigma, Cat#V900445), hydroxocobalamin (OH-B12, Sigma, H1428000), methyl-cobalamin (met-B12, Sigma, Cat#M9756), and adenosyl-cobalamin (ado-B12, Sigma, Cat#C0884) were dissolved in water to prepare 15 mM stock solution, which were subsequently diluted to 2 nM working solutions. The met-B12 and ado-B12were used as the reference standards for LC-MS/MS. Sodium acetate (Sigma, Cat#S5636) and sodium acrylate

(Sigma, Cat#408220) were dissolved in water as 2 M stock solutions and diluted to 100 mM working solutions. To prevent bacterial consumption, all metabolites except B12 were supplied directly in the CeHR medium unless otherwise stated.

Human cell lines and culture conditions

Huh7 cells were passaged in Dulbecco's Modified Eagle Medium (DMEM, Sigma, Cat#D6429) supplemented with 10% (v/v) fetal bovine serum (FBS, Gibco, Cat#10099141). Cell proliferation was measured as previously described[50]. In the methionine-free media (Thermo Fisher, Cat#21013024), 1.5 μM cyanocobalamin, 4 mM L-glutamine (Sigma, Cat#G7513), 200 μM L-cysteine (Sigma, Cat#C7352) were added in all groups, and either 200 μM L-methionine (Sigma, Cat#M5308) or L-HCY (Sigma, Cat#69453) were added as indicated.

Isolation and culture of primary hepatocytes

Primary hepatocytes were isolated from 7- to 12-week-old male mice using a modified two-step collagenase perfusion method. In brief, the mouse liver was first perfused with 50 mL of HBSS buffer containing 0.5 mM EGTA, followed by perfusion with 50 mL of HBSS supplemented with 5 mM $CaCl_2$ and 0.5 mg/mL collagenase type IV (Sigma, Cat#C5138). Liberated hepatocytes were collected, washed with cold M199 medium, filtered through a 70-μm cell strainer, and centrifuged at 50 × g for 5 min at 4 °C. The cell pellet was resuspended in 20 mL of cold M199 medium, mixed with 20 mL of Percoll, and subjected to gradient centrifugation at 270 × g for 5 min at 4 °C. The hepatocyte pellet obtained at the bottom was washed once with cold M199 medium and resuspended in fresh M199 medium. Only hepatocytes exhibiting greater than 90% viability, as determined by trypan blue exclusion, were used for subsequent experiments. The isolated hepatocytes were seeded at a density of 2.5×10^5 cells/mL in 12-well plates or 1.5×10^6 cells per

6 cm dish on rat tail collagen type I-coated surfaces, using M199 culture medium supplemented with 10% FBS, 1% penicillin/streptomycin, and 100 nM dexamethasone. After 4–5 h of attachment, the medium was replaced with fresh medium, and cells were treated with either vehicle or 3-FP (2 mM) for 24 h prior to sample collection for total RNA extraction or LC-MS analysis.

Feeding RNAi in *C. elegans*

RNAi feeding experiments were conducted on synchronized L1 larvae, which were obtained by bleach treatment of gravid adults, and plated onto the RNAi bacterial lawns. The RNAi bacterial strains, sourced from the genomic Ahringer library and the ORFeome-based Vidal library, were grown overnight, seeded onto NGM plates supplemented with 5 mM IPTG (Lablead, Cat#0487) and 100 μg/mL carbenicillin. After drying in a laminar flow cabinet, plates were incubated overnight at room temperature for induction.

Imaging of the fluorescence in worms

The transcriptional reporter strain *acdh-1p::GFP* was used for indicating endogenous B12 status. To observe the subcellular localization of NHR-68 and NHR-10, *nhr-68p::nhr-68::RFP* and *nhr-10p::nhr-10::RFP* translational fusion strains were used. For mitochondrial staining, *C. elegans* were incubated overnight in the dark at 20 °C on NGM plates containing 2 μM cationic Nile blue (CNB) before observation[51]. Worms were anesthetized in M9 containing 40 mM NaN_3 and mounted on either agar pads or glass slides for imaging. The images were acquired using a Leica DM500 microscope with consistent exposure settings across samples.

For quantification, the fluorescence intensity of GFP or RFP in the nucleus (in arbitrary units, a.u.) was calculated by ImageJ software with subtraction of the background next to the same nucleus.

Data are presented as relative fluorescence units normalized to the average fluorescence intensity of the control animals.

Developmental staging assay

The developmental state of a population was measured by synchronizing animals by L1 arrest in M9 for 20 h, then allowing animals to develop at 20°C under various dietary conditions for indicated periods. Approximately 50 animals were visually categorized on a dissecting microscope into age groups based on well-defined morphological landmarks, primarily focusing on the development of the vulva and germline morphology as described[27]. Data are presented as the percentage distribution of animals at each stage.

Brood size measurement

Synchronized L1 worms were cultured on plates seed with indicated RNAi bacteria for 48 hours before being individually transferred into a new plate with consistent bacteria. The individual worms were transferred to new plates every day, and the number of offspring was counted until no more eggs were laid. The total brood size per worm was defined as the cumulative number of viable progenies counted across all plates.

Assessment of detoxification via offspring viability

The detoxification capacity of B12 was assessed using an offspring survival assay, adapted from a previously established protocol[23]. Briefly, approximately 5 synchronized P0 worms were transferred to the B12-deficient NGM plate seeded with RNAi bacteria cultured in B12-deficient LB, treated with or without 2 nM B12. Offspring viability was monitored at the indicated time points.

435

436 **EMS mutagenesis and mutant identification**

437 Synchronized L4-stage *pdha-1 (aly3); wwIs24 [acdh-1p::GFP + unc-119(+)]* animals were
438 subjected to chemical mutagenesis using ethyl methanesulfonate (EMS) according to standard
439 protocols[52]. Briefly, worms were treated with 0.5% EMS for 4 h. Putative suppressor mutants were
440 isolated from the F2 generation based on visually reduced GFP fluorescence.

441

442 To eliminate background mutations, each candidate was outcrossed to parental strain for three
443 generations. Whole genome Illumina sequencing was employed followed by analysis and variant
444 calling in Galaxy[53] to identify causal mutations. Causal mutations were confirmed by Sanger
445 sequencing and RNAi.

446

447 **RNA extraction and quantitative RT-PCR**

448 Total RNA from synchronized young adult worms was extracted with an Easy RNA kit (Easy-do,
449 Cat#DR0401050). The removal of gDNA and reverse transcription of worm RNA were performed
450 with HiScript III RT SuperMix for qPCR (+gDNA wiper) (Vazyme, Cat#R323). Quantitative PCR
451 was conducted with ChamQ Universal SYBR qPCR Master Mix (Vazyme, Cat#Q711) on a
452 quantitative PCR system (Jena Qtower 3G). The expression levels of genes of interest were
453 normalized to those of *act-1*.

454

455 **RNA-seq and analysis**

456 RNA was extracted with TRIzol reagent (Life Technologies). The RNA quality and quantity were
457 determined with a NanoPhotometer® spectrophotometer (IMPLEN) and a Qubit® RNA Assay

Kit in a Qubit® 2.0 Fluorometer (Life Technologies). The integrity of the RNA was assessed using the RNA Nano 6000 Assay Kit of a Bioanalyzer 2100 system (Agilent).

Sequencing libraries were generated using an NEBNext® Ultra™ RNA Library Prep Kit for Illumina® (NEB, USA) following the manufacturer's recommendations, and index codes were added to attribute sequences to each sample. Clustering of the index-coded samples was performed on a cBot Cluster Generation System using a TruSeq PE Cluster Kit v3-cBot-HS (Illumina) according to the manufacturer's instructions. After cluster generation, the library preparations were sequenced on an Illumina platform, and 125 bp/150 bp paired-end reads were generated. The sequencing reads were demultiplexed (bcl2fastq) and quantified with kallisto 0.46.0 with the default parameters according to the WormBase reference genome (WS245).

Differential gene expression analysis was performed using DESeq2 1.26.0, and only false discovery rate (FDR)-adjusted *p* values less than 0.05 were considered to indicate statistical significance. The variance-stabilizing transformed counts were used for heatmap plots. For functional enrichment analysis of gene clusters, GO analyses were performed with g:Profiler[54]

PDC activity measurement

The synchronized young adult N2 and *pdha-1*^{A111V} mutants were collected and washed 3 times with M9 buffer and once with sterile ddH2O, and then sonicated with a Bioruptor sonication device using a program of 10 s on/ 10 s off for 30 cycles, repeated 6 times on ice. The enzymatic activity of PDC was detected using Pyruvate Dehydrogenase (PDH) Activity Assay Kit (Bioleaper, Cat# BR5000639) according to its protocols. The measured PDC activity was normalized to the protein levels of each group.

482

483 **Whole blood sample collection and preparation**

484 This retrospective case-control study utilized archived blood samples from PDCD patients and
485 health controls, which were collected from four independent hospitals (Supplementary Table 1).
486 Detailed demographic and clinical information, including patient ID, specific genetic mutation
487 sites, sex, and age, is comprehensively summarized in Supplementary Table 1. Healthy controls
488 were selected to match the overall age and sex distribution of the patient cohort, although age
489 discrepancies exist for 2 individual matched pairs. No additional selection criteria were applied
490 beyond genetic confirmation. The study protocol was specifically reviewed and approved by the
491 ethics committee of Westlake University (Approval No.: 20260129DD001). As the samples were
492 pre-existing and fully anonymized, the requirement for individual informed consent was waived
493 by the ethics committees, in compliance with national regulations and the Declaration of Helsinki.
494 Peripheral whole blood samples were collected from all participants using standard clinical
495 vacuum blood collection tubes containing EDTA as an anticoagulant, and were immediately stored
496 at -80°C. During transportation between facilities, samples were maintained on dry ice to ensure
497 stability. Metabolite levels in the samples were subsequently quantified using LC-MS/MS.

498

499 **LC-MS/MS quantification**

500 The levels of metabolites in *C. elegans*, mouse primary hepatocytes and human blood samples
501 were determined by LC-MS/MS. Samples were collected in 80% ice methanol before being
502 sonification described above. After sonification, the samples were stored at -80 °C overnight (*C.*
503 *elegans* and mouse primary hepatocytes) or at 4 °C for 30 min (human blood samples), for
504 metabolite extraction. The samples were then centrifuged at the maximum speed for 10 min at 4 °C.
505 The pellet was resuspended in 1% SDS to measure protein levels with a BCA protein assay

(Thermo Fisher). The supernatant was collected, lyophilized and resuspended in 100 μL 80% methanol for LC-MS/MS detection.

The metabolome analysis was conducted using an LC-MS system comprising an Agilent 1290 Infinity II UHPLC system tandem with Agilent 6545 Q-TOF/MS (Agilent). Chromatographic separation was achieved on an ACQUITY UPLC BEH Amide column (100mm×2.1 mm, 1.7 μm). The mobile phase consisted of 15mM ammonium acetate, 0.3% NH3·H20 in water (A) and 15mM ammonium acetate, 0.3% NH3·H20 in 9:1 acetonitrile/water (B) at a flow rate of 0.3 ml/min. The column was eluted with 95% mobile phase B for 1 minute, followed by a linear gradient to 50% mobile-phase B over 8 min, held at 50% for 3 min, a linear gradient to 95% mobile phase B over 0.5 min, then 1.5 min at 95% mobile-phase B. The sample volume injected was 5 μL.

MS data were acquired using electrospray ionization in both positive and negative ion mode over 50–1250 m/z. Other MS settings include: sheath gas temperature 350℃, sheath gas flow 11 L/min, VCap 4000 V, Nozzle voltage 1000 V, gas temperature 350℃, nebulizer gas 30 psi; Drying gas flow rate 8 L/min; fragmentor 110 V, skimmer 65 V. Raw data were processed using Profinder 10.0 (Agilent) for peak detection, alignment and integration.

The targeted LC-MS/MS analysis was conducted using an Agilent 1290 Infinity II UHPLC system tandem with Agilent 6495 mass spectrometer. All data were collected and processed using QQQ Quantitative Analysis Software. Chromatographic separation was achieved on ACQUITY UPLC BEH Amide column (100mm×2.1 mm, 1.7 μm) column. The mobile phase consisted of 15mM ammonium acetate, 0.3% NH3·H20 in water (A) and 15mM ammonium acetate, 0.3% NH3·H20 in 9:1 acetonitrile/water (B) at a flow rate of 0.3 ml/min. The column was eluted with 90% mobile

phase B for 1 minute, followed by a linear gradient to 50% mobile-phase B over 4 min, held at 50% for 3 min, a linear gradient to 90% mobile phase B over 0.1 min, then 3.9 min at 90% mobile-phase B. The sample volume injected was 2 μL. Mass spectrometer using the following settings: gas temperature 200°C, gas flow 14 l/min, Nebulizer 20 psi, Sheath gas temperature 350°C, Sheath gas flow 11 l/min, Capillary 3000V, Nozzle Voltage 1500V. The quantitative analysis of all compounds was measured by multiple reaction monitoring (MRM) mode. Ado_B12, met_B12 and acetyl-COA were measured in positive ion mode, the MRM transitions used were as follows, m/z of ado-B12 was 790.01/146.9, m/z of met-B12 was 673/147, m/z of acetyl-COA was 810.1/303.1. Lactate was measured in negative ion mode, the m/z was 89/43.1. The relative levels of metabolites were determined based on the area under the curve (AUC), normalized first to total protein and subsequently to the average levels in control animals.

For HCY detection, Chromatographic separation was achieved on ACQUITY UPLC BEH Amide column (100mm×2.1 mm, 1.7 μm) column. The mobile phase consisted of 10mM ammonium acetate, 0.2% FA in water (A) and acetate (B) at a flow rate of 0.3 ml/min. The column was eluted with 90% mobile phase B for 1 minute, followed by a linear gradient to 50% mobile-phase B over 4 min, held at 50% for 3 min, a linear gradient to 90% mobile phase B over 0.1 min, then 3.9 min at 90% mobile-phase B. The sample volume injected was 2 μL. Mass spectrometer operating in positive ion mode using the following settings: gas temperature 200°C, gas flow 14 l/min, Nebulizer 20 psi, Sheath gas temperature 350°C, Sheath gas flow 11 l/min, Capillary 3000V, Nozzle Voltage 1500V. The quantitative analysis of HCY was measured by multiple reaction monitoring (MRM) mode. The MRM transitions was m/z 136.05→89.9, and the dwell time was set at 100 ms.

For MMA detection, Chromatographic separation was achieved on Waters ACQUITY UPLC HSS T3 (100 mm × 2.1 mm, 1.8 μm) column. The mobile phase consisted of 0.1%(v/v) formic acid in water as solvent A and 0.1%(v/v) formic acid in methanol as solvent B at a flow rate of 0.3 mL/min. The gradient of mobile phase B was 2% in 1 min, 2% to 15% in 2 min, 15% to 50% in 1 min, 50% to 95% in 1 min, held at 95% for 3 min, then 95% to 2% in 0.1 min, held at 2% for 3.9 min. The flow rate of mobile phase was kept at 0.3 mL/min, column temperature was set at 40°C and the injection volume was 2 μL. Mass spectrometer operating in negative ion mode using the following settings: gas temperature 200°C, gas flow 14 l/min, Nebulizer 40 psi, Sheath gas temperature 400°C, Sheath gas flow 11 l/min, Capillary 3000V, Nozzle Voltage 500V. The quantitative analysis of MMA was measured by multiple reaction monitoring (MRM) mode. The MRM transitions used was m/z 117→55, and the dwell time was set at 100 ms.

Stable isotope tracing experiments

U-$^{13}C_6$ glucose tracing

Isotope tracing experiments using uniformly labeled $^{13}C_6$ glucose (U-$^{13}C_6$ glucose; Cambridge Isotope Laboratories, CIL-CLM-1396) were performed following established protocols [55]. Synchronized worms were cultured in CeHR medium from the L1 larval stage and harvested at the young adult stage.. U-$^{13}C_6$ glucose (72.5 mM) was substituted for the equivalent concentration of unlabeled glucose in CeHR medium beginning at the L1 stage. Metabolite extraction and LC–MS/MS detection were performed as described for metabolome analysis in the “LC–MS/MS quantification” section.

U-$^{13}C_3$ propionate tracing

Isotope tracing experiments using uniformly labeled $^{13}C3$ sodium propionate (U-$^{13}C_3$ sodium propionate; Cambridge Isotope Laboratories, CIL-CLM-1865) were conducted based on published methods [56]. Synchronized worms were cultured in CeHR medium and harvested at the young adult stage. U-$^{13}C_3$ sodium propionate (50 mM) was administered 8 h prior to collection. Metabolites were extracted as described above. ^{13}C-labeled metabolites were quantified by targeted using previously established methods LC–MS/MS [57,58], with parent-and-daughter ions transitions specific to the ^{13}C-labeled form of each metabolite. Chromatographic separation was performed on a SeQuant Zic-hydrophilic interaction liquid chromatography (pHILIC) column (5 μm polymer 150 × 2.1 mm; MilliporeSigma), interfaced with a high-performance LC system (ExionLC AD System) coupled to a triple quadrupole mass spectrometer (QTRAP 6500 + System; AB SCIEX). A 34-min gradient elution was conducted at a flow rate of 0.15 mL/min with mobile phase A consisting of 20 mM ammonium acetate and 0.1% (v/v) ammonium hydroxide in water, and mobile phase B consisting of 100% acetonitrile. The gradient program was as follows: 80% B at 0–0.01 min, linear decrease to 20% B over 20 min, return to 80% B at 20.5 min, and hold at 80% B until 34 min for column re-equilibration. Metabolites were detected using multiple reaction monitoring (MRM) transitions in both positive and negative ionization modes.

Automated metabolic flux analysis

Metabolic network construction

A comprehensive metabolic network was assembled encompassing central carbon metabolism pathways, including glycolysis, the tricarboxylic acid (TCA) cycle, pentose phosphate pathway, one-carbon metabolism, and amino acid biosynthetic routes, following established modeling frameworks[59].

Mass isotopomer distribution data processing

To account for technical variability across experimental batches, mass isotopomer distribution (MID) measurements were consolidated by computing the mean values across biological replicates for each metabolite. Flux estimation was performed using an iterative prediction-optimization framework. For each metabolite i, the theoretical MID vector ($\widetilde{\boldsymbol{M}}_i$) was calculated as a flux-weighted linear combination of its biosynthetic precursor MIDs:

$$\widetilde{\boldsymbol{M}}_i = \frac{\sum_{\forall j} v_{ji} \boldsymbol{M}_{ji}}{\sum_{\forall j} v_{ji}}$$

where v_{ji} represents the metabolic flux from precursor j to product i, and $\boldsymbol{M}_{ji}$ denotes the MID vector of j-derived metabolite i. For metabolites whose precursor MIDs remained undefined, this calculation was applied recursively until all upstream MID vectors were resolved.

Constrained optimization framework

Model fitting was achieved by minimizing the discrepancy between experimental and predicted MID profiles. The objective function quantified this deviation using weighted sum-of-squared residuals:

$$SSE_i = \left\| \widetilde{\boldsymbol{M}}_i - \boldsymbol{M}_i \right\|^2 = \sum_m \left(\widetilde{M}_{i,m} - M_{i,m} \right)^2$$

where m indexes individual isotopomer species within the MID vector. The global objective function aggregated residuals across all measured metabolites:

$$\min_{\boldsymbol{v}} L_{\text{total}}(\boldsymbol{v}) = \sum_i SSE_i$$

s.t. $\boldsymbol{A} \cdot \boldsymbol{v}^T = \boldsymbol{b}$, $\boldsymbol{0} \leq \boldsymbol{v}_{\min} \leq \boldsymbol{v} \leq \boldsymbol{v}_{\max}$

where $\boldsymbol{A}$ represents the stoichiometric matrix encoding mass balance constraints, $\boldsymbol{b}$ is the net production/consumption vector, $\boldsymbol{v}$ is the flux vector, and $\boldsymbol{v}_{\min}$ and $\boldsymbol{v}_{\max}$ denote lower and upper

622 flux boundaries, respectively. This constrained nonlinear optimization was solved using sequential
623 quadratic programming[60] within the Elementary Metabolite Units (EMU) computational
624 framework[61].
625
626 ***Solution ensemble and uncertainty quantification***
627 To ensure solution robustness and mitigate the risk of convergence to local minima, MFA solutions
628 underwent an optimization-selection-averaging procedure following our previous report[59]. Briefly,
629 the optimization was executed 20,000 times with randomized initial flux distributions sampled
630 uniformly within the feasible flux space. The 100 solutions with the lowest objective function
631 values were selected and grouped into five subsets of 20 solutions each. Each subset was averaged
632 to generate one representative solution, yielding five final solutions from which consensus flux
633 estimates and associated confidence intervals were derived.
634
635 **Oxygen consumption rate measurement**
636 Mitochondrial respiration was assessed by measuring the OCR using a Seahorse XF Pro analyzer
637 (Agilent). Synchronized young adult worms were transferred into individual wells of a 96-well
638 assay plate. To evaluate mitochondrial function, the uncoupler carbonyl cyanide-4-
639 (trifluoromethoxy)phenylhydrazone (FCCP; final concentration 10 μM; Sigma-Aldrich, C2920)
640 was injected to induce maximal respiratory capacity, followed by the addition of sodium azide
641 (NaN_3; final concentration 40 mM) to inhibit complexes IV and V of the electron transport chain,
642 thereby allowing determination of non-mitochondrial respiration. Basal OCR was calculated as
643 the average OCR before FCCP injection minus the minimum OCR after NaN_3 treatment.
644
645 **Quantification and statistical analysis**

GraphPad Prism 8.0 (GraphPad Software, Inc.) was used for statistical analyses in this study. Differences between two groups were analyzed by unpaired *t* test. For differences among multiple groups, one-way analysis of variance (ANOVA) followed by Tukey's test was used. Differences between multiple groups with two variations were analyzed by two-way ANOVA. The significance of significant differences is indicated as $*p < 0.05$, $**p < 0.01$, and $***p < 0.001$, ns, not significant. The error bars are the SEM. Biological replicates for each experiment can be found in Figure legends.

Data, code, and materials availability

All data are available in the main text or the supplementary materials. RNA-seq data have been deposited in NCBI's Sequence Read Archive (SRA) with accession no. PRJNA1417761. The source code and processed data for isotope tracing and metabolic flux analysis are publicly available at https://github.com/cmplab-cimr/2026_LianfengWu_roundworm_MFA.

References

1 Stacpoole, P. W. & McCall, C. E. The pyruvate dehydrogenase complex: Life's essential, vulnerable and druggable energy homeostat. *Mitochondrion* **70**, 59-102, doi:10.1016/j.mito.2023.02.007 (2023).

2 Ganetzky, R., McCormick, E. M. & Falk, M. J. in *GeneReviews((R))* (eds M. P. Adam *et al.*) (1993).

3 Ebertowska, A., Ludkiewicz, B., Klejbor, I., Melka, N. & Morys, J. Pyruvate dehydrogenase deficiency: morphological and metabolic effects, creation of animal model to search for curative treatment. *Folia Morphol (Warsz)* **79**, 191-197, doi:10.5603/FM.a2020.0020 (2020).

4 DeBrosse, S. D., Okajima, K., Zhang, S., Nakouzi, G., Schmotzer, C. L. *et al.* Spectrum of neurological and survival outcomes in pyruvate dehydrogenase complex (PDC) deficiency: lack of correlation with genotype. *Mol Genet Metab* **107**, 394-402, doi:10.1016/j.ymgme.2012.09.001 (2012).

5 Verma, A., Lehman, A. N., Gokcan, H., Cropcho, L., Black, D. *et al.* Amino acid ratio combinations as biomarkers for discriminating patients with pyruvate dehydrogenase complex deficiency from other inborn errors of metabolism. *Mol Genet Genomic Med* **12**, e2283, doi:10.1002/mgg3.2283 (2024).

6 Jakkamsetti, V., Marin-Valencia, I., Ma, Q., Good, L. B., Terrill, T. *et al.* Brain metabolism modulates neuronal excitability in a mouse model of pyruvate dehydrogenase deficiency. *Sci Transl Med* **11**, doi:10.1126/scitranslmed.aan0457 (2019).

7 Patel, M. S., Mahmood, S., Jung, J. & Rideout, T. C. Reprogramming of aerobic glycolysis in non-transformed mouse liver with pyruvate dehydrogenase complex deficiency. *Physiol Rep* **9**, e14684, doi:10.14814/phy2.14684 (2021).

8 Sidhu, S., Gangasani, A., Korotchkina, L. G., Suzuki, G., Fallavollita, J. A. *et al.* Tissue-specific pyruvate dehydrogenase complex deficiency causes cardiac hypertrophy and sudden death of weaned male mice. *Am J Physiol Heart Circ Physiol* **295**, H946-H952, doi:10.1152/ajpheart.00363.2008 (2008).

9 Gopal, K., Abdualkader, A. M., Li, X., Greenwell, A. A., Karwi, Q. G. *et al.* Loss of muscle PDH induces lactic acidosis and adaptive anaplerotic compensation via pyruvate-alanine cycling and glutaminolysis. *J Biol Chem* **299**, 105375, doi:10.1016/j.jbc.2023.105375 (2023).

10 Taylor, M. R., Hurley, J. B., Van Epps, H. A. & Brockerhoff, S. E. A zebrafish model for pyruvate dehydrogenase deficiency: rescue of neurological dysfunction and embryonic lethality using a ketogenic diet. *Proc Natl Acad Sci U S A* **101**, 4584-4589, doi:10.1073/pnas.0307074101 (2004).

11 Green, R., Allen, L. H., Bjorke-Monsen, A. L., Brito, A., Gueant, J. L. *et al.* Vitamin B(12) deficiency. *Nat Rev Dis Primers* **3**, 17040, doi:10.1038/nrdp.2017.40 (2017).

12 Qin, S., Wang, Y., Li, L., Liu, J., Xiao, C. *et al.* Early-life vitamin B12 orchestrates lipid peroxidation to ensure reproductive success via SBP-1/SREBP1 in Caenorhabditis elegans. *Cell Rep* **40**, 111381, doi:10.1016/j.celrep.2022.111381 (2022).

13 Carmel, R. Biomarkers of cobalamin (vitamin B-12) status in the epidemiologic setting: a critical overview of context, applications, and performance characteristics of cobalamin, methylmalonic acid, and holotranscobalamin II. *Am J Clin Nutr* **94**, 348S-358S, doi:10.3945/ajcn.111.013441 (2011).

14 Solomon, L. R. Functional cobalamin (vitamin B12) deficiency: role of advanced age and disorders associated with increased oxidative stress. *Eur J Clin Nutr* **69**, 687-692, doi:10.1038/ejcn.2014.272 (2015).

15 Zhu, S., Zhang, R., Yao, L., Lin, Z., Li, Y. *et al.* De novo NAD(+) synthesis is ineffective for NAD(+) supply in axenically cultured Caenorhabditis elegans. *Commun Biol* **8**, 545, doi:10.1038/s42003-025-07984-2 (2025).

16 Li, Y., Duan, D., Zhu, S., Liu, Z., Zhang, Q. *et al.* Genome-wide RNAi screening in C. elegans reveals OXPHOS and pyrimidine synthesis pathways as PKA regulators. *Commun Biol* **8**, 1280, doi:10.1038/s42003-025-08718-0 (2025).

17 Qin, C., Liu, Z., Duan, D. & Wu, L. Genome-wide RNAi analysis in adult Caenorhabditis elegans unveils genes controlling age-related fat accumulation. *Mech Ageing Dev* **226**, 112089, doi:10.1016/j.mad.2025.112089 (2025).

18 Li, X., Zhang, H., Hodder, T., Wang, W., Myers, C. L. *et al.* Systems-level design principles of metabolic rewiring in an animal. *Nature* **640**, 203-211, doi:10.1038/s41586-025-08636-5 (2025).

19 Wei, W. & Ruvkun, G. Lysosomal activity regulates Caenorhabditis elegans mitochondrial dynamics through vitamin B12 metabolism. *Proc Natl Acad Sci U S A* **117**, 19970-19981, doi:10.1073/pnas.2008021117 (2020).

20 Patel, M. S., Nemeria, N. S., Furey, W. & Jordan, F. The pyruvate dehydrogenase complexes: structure-based function and regulation. *J Biol Chem* **289**, 16615-16623, doi:10.1074/jbc.R114.563148 (2014).

21 Merkevicius, K., Smirnov, D., Schlieben, L. D., Ganetzky, R., Feichtinger, R. G. *et al.* The genotypic and phenotypic landscape of PDHA1-related pyruvate dehydrogenase complex deficiency. *Brain*, doi:10.1093/brain/awaf430 (2025).

22 Patel, K. P., O'Brien, T. W., Subramony, S. H., Shuster, J. & Stacpoole, P. W. The spectrum of pyruvate dehydrogenase complex deficiency: clinical, biochemical and genetic features in 371 patients. *Mol Genet Metab* **105**, 34-43, doi:10.1016/j.ymgme.2011.09.032 (2012).

23 Watson, E., Olin-Sandoval, V., Hoy, M. J., Li, C. H., Louisse, T. *et al.* Metabolic network rewiring of propionate flux compensates vitamin B12 deficiency in C. elegans. *Elife* **5**, doi:10.7554/eLife.17670 (2016).

24 Bulcha, J. T., Giese, G. E., Ali, M. Z., Lee, Y. U., Walker, M. D. *et al.* A Persistence Detector for Metabolic Network Rewiring in an Animal. *Cell Rep* **26**, 460-468 e464, doi:10.1016/j.celrep.2018.12.064 (2019).

25 Zhou, J., Duan, M., Wang, X., Zhang, F., Zhou, H. *et al.* A feedback loop engaging propionate catabolism intermediates controls mitochondrial morphology. *Nat Cell Biol* **24**, 526-537, doi:10.1038/s41556-022-00883-2 (2022).

26 Na, H., Ponomarova, O., Giese, G. E. & Walhout, A. J. M. C. elegans MRP-5 Exports Vitamin B12 from Mother to Offspring to Support Embryonic Development. *Cell Rep* **22**, 3126-3133, doi:10.1016/j.celrep.2018.02.100 (2018).

27 Watson, E., MacNeil, L. T., Ritter, A. D., Yilmaz, L. S., Rosebrock, A. P. *et al.* Interspecies systems biology uncovers metabolites affecting C. elegans gene expression and life history traits. *Cell* **156**, 759-770, doi:10.1016/j.cell.2014.01.047 (2014).

28 Vashi, P., Edwin, P., Popiel, B., Lammersfeld, C. & Gupta, D. Methylmalonic Acid and Homocysteine as Indicators of Vitamin B-12 Deficiency in Cancer. *PLoS One* **11**, e0147843, doi:10.1371/journal.pone.0147843 (2016).

29 Hannibal, L., Lysne, V., Bjorke-Monsen, A. L., Behringer, S., Grunert, S. C. *et al.* Biomarkers and Algorithms for the Diagnosis of Vitamin B12 Deficiency. *Front Mol Biosci* **3**, 27, doi:10.3389/fmolb.2016.00027 (2016).

30 Yao, L., Wang, Y., Qin, S., Zhu, S. & Wu, L. The antidiabetic drug metformin aids bacteria in hijacking vitamin B12 from the environment through RcdA. *Commun Biol* **6**, 96, doi:10.1038/s42003-023-04475-0 (2023).

31 Chen, J., Guccini, I., Di Mitri, D., Brina, D., Revandkar, A. *et al.* Compartmentalized activities of the pyruvate dehydrogenase complex sustain lipogenesis in prostate cancer. *Nat Genet* **50**, 219-228, doi:10.1038/s41588-017-0026-3 (2018).

32 Husseiny, M. & Nilsson, R. The role of B(12) deficiency and methionine synthase in methionine-dependent cancer cells. *Cancer Metab* **13**, 34, doi:10.1186/s40170-025-00405-2 (2025).

33 Goh, G. Y. S., Beigi, A., Yan, J., Doering, K. R. S. & Taubert, S. Mediator subunit MDT-15 promotes expression of propionic acid breakdown genes to prevent embryonic lethality in Caenorhabditis elegans. *G3 (Bethesda)* **13**, doi:10.1093/g3journal/jkad087 (2023).

34 Shen, H., Campanello, G. C., Flicker, D., Grabarek, Z., Hu, J. *et al.* The Human Knockout Gene CLYBL Connects Itaconate to Vitamin B(12). *Cell* **171**, 771-782 e711, doi:10.1016/j.cell.2017.09.051 (2017).

35 Griffith, C. M., Conrotte, J. F., Paydar, P., Xie, X., Heins-Marroquin, U. *et al.* CLYBL averts vitamin B(12) depletion by repairing malyl-CoA. *Nat Chem Biol* **21**, 906-915, doi:10.1038/s41589-025-01857-9 (2025).

36 Ruetz, M., Campanello, G. C., Purchal, M., Shen, H., McDevitt, L. *et al.* Itaconyl-CoA forms a stable biradical in methylmalonyl-CoA mutase and derails its activity and repair. *Science* **366**, 589-593, doi:10.1126/science.aay0934 (2019).

37 Liu, S. & Locasale, J. W. Flux measurements of the tricarboxylic acid cycle in the tumors of mice. *Life Metab* **2**, load020, doi:10.1093/lifemeta/load020 (2023).

38 Chuang, M. H., Chiou, S. H., Huang, C. H., Yang, W. B. & Wong, C. H. The lifespan-promoting effect of acetic acid and Reishi polysaccharide. *Bioorg Med Chem* **17**, 7831-7840, doi:10.1016/j.bmc.2009.09.002 (2009).

39 Edwards, C., Canfield, J., Copes, N., Brito, A., Rehan, M. *et al.* Mechanisms of amino acid-mediated lifespan extension in Caenorhabditis elegans. *BMC Genet* **16**, 8, doi:10.1186/s12863-015-0167-2 (2015).

40 Yang, M. & Du, Z. Reaffirming the value of model organisms in training scientific minds. *Nat Cell Biol* **27**, 1589-1591, doi:10.1038/s41556-025-01754-2 (2025).

41 Stabler, S. P. & Allen, R. H. Vitamin B12 deficiency as a worldwide problem. *Annu Rev Nutr* **24**, 299-326, doi:10.1146/annurev.nutr.24.012003.132440 (2004).

42 Suliman, H. S., Sawyer, G. M., Appling, D. R. & Robertus, J. D. Purification and properties of cobalamin-independent methionine synthase from Candida albicans and Saccharomyces cerevisiae. *Arch Biochem Biophys* **441**, 56-63, doi:10.1016/j.abb.2005.06.016 (2005).

43 Young, D. B., Comas, I. & de Carvalho, L. P. Phylogenetic analysis of vitamin B12-related metabolism in Mycobacterium tuberculosis. *Front Mol Biosci* **2**, 6, doi:10.3389/fmolb.2015.00006 (2015).

44 Yang, F., Vought, B. W., Satterlee, J. S., Walker, A. K., Jim Sun, Z. Y. *et al.* An ARC/Mediator subunit required for SREBP control of cholesterol and lipid homeostasis. *Nature* **442**, 700-704, doi:10.1038/nature04942 (2006).

45 Goh, G. Y., Martelli, K. L., Parhar, K. S., Kwong, A. W., Wong, M. A. *et al.* The conserved Mediator subunit MDT-15 is required for oxidative stress responses in Caenorhabditis elegans. *Aging Cell* **13**, 70-79, doi:10.1111/acel.12154 (2014).

46 Zhang, Y., Shen, X., Shen, Y., Wang, C., Yu, C. *et al.* Cytosolic acetyl-coenzyme A is a signalling metabolite to control mitophagy. *Nature* **649**, 1022-1031, doi:10.1038/s41586-025-09745-x (2026).

47 Avula, S., Parikh, S., Demarest, S., Kurz, J. & Gropman, A. Treatment of mitochondrial disorders. *Curr Treat Options Neurol* **16**, 292, doi:10.1007/s11940-014-0292-7 (2014).

48 Brenner, S. The genetics of Caenorhabditis elegans. *Genetics* **77**, 71-94, doi:10.1093/genetics/77.1.71 (1974).

49 Samuel, T. K., Sinclair, J. W., Pinter, K. L. & Hamza, I. Culturing Caenorhabditis elegans in axenic liquid media and creation of transgenic worms by microparticle bombardment. *J Vis Exp*, e51796, doi:10.3791/51796 (2014).

50 Booher, K., Lin, D. W., Borrego, S. L. & Kaiser, P. Downregulation of Cdc6 and pre-replication complexes in response to methionine stress in breast cancer cells. *Cell Cycle* **11**, 4414-4423, doi:10.4161/cc.22767 (2012).

51 Zhang, R., Fang, J., Qi, T., Zhu, S., Yao, L. *et al.* Maternal aging increases offspring adult body size via transmission of donut-shaped mitochondria. *Cell Res* **33**, 821-834, doi:10.1038/s41422-023-00854-8 (2023).

52 Wu, L., Zhou, B., Oshiro-Rapley, N., Li, M., Paulo, J. A. *et al.* An Ancient, Unified Mechanism for Metformin Growth Inhibition in C. elegans and Cancer. *Cell* **167**, 1705-1718 e1713, doi:10.1016/j.cell.2016.11.055 (2016).

53 Kim, E., Goraksha-Hicks, P., Li, L., Neufeld, T. P. & Guan, K. L. Regulation of TORC1 by Rag GTPases in nutrient response. *Nat Cell Biol* **10**, 935-945, doi:10.1038/ncb1753 (2008).

54 Kolberg, L., Raudvere, U., Kuzmin, I., Adler, P., Vilo, J. *et al.* g:Profiler-interoperable web service for functional enrichment analysis and gene identifier mapping (2023 update). *Nucleic Acids Res* **51**, W207-W212, doi:10.1093/nar/gkad347 (2023).

55 Falk, M. J., Rao, M., Ostrovsky, J., Daikhin, E., Nissim, I. *et al.* Stable isotopic profiling of intermediary metabolic flux in developing and adult stage Caenorhabditis elegans. *J Vis Exp*, doi:10.3791/2288 (2011).

56 Zhu, Y., Tong, X., Xue, J., Qiu, H., Zhang, D. *et al.* Phospholipid biosynthesis modulates nucleotide metabolism and reductive capacity. *Nat Chem Biol* **21**, 35-46, doi:10.1038/s41589-024-01689-z (2025).

57 Ye, C., Sutter, B. M., Wang, Y., Kuang, Z. & Tu, B. P. A Metabolic Function for Phospholipid and Histone Methylation. *Mol Cell* **66**, 180-193 e188, doi:10.1016/j.molcel.2017.02.026 (2017).

58 Ye, C., Sutter, B. M., Wang, Y., Kuang, Z., Zhao, X. *et al.* Demethylation of the Protein Phosphatase PP2A Promotes Demethylation of Histones to Enable Their Function as a Methyl Group Sink. *Mol Cell* **73**, 1115-1126 e1116, doi:10.1016/j.molcel.2019.01.012 (2019).

59 Liu, S., Liu, X. & Locasale, J. W. Quantitation of metabolic activity from isotope tracing data using automated methodology. *Nat Metab* **6**, 2207-2209, doi:10.1038/s42255-024-01144-2 (2024).

60 Kraft, D. A software package for sequential quadratic programming. *Forschungsbericht-Deutsche Forschungs- und Versuchsanstalt fur Luft- und Raumfahrt* (1988).

61 Antoniewicz, M. R., Kelleher, J. K. & Stephanopoulos, G. Elementary metabolite units (EMU): a novel framework for modeling isotopic distributions. *Metab Eng* **9**, 68-86, doi:10.1016/j.ymben.2006.09.001 (2007).

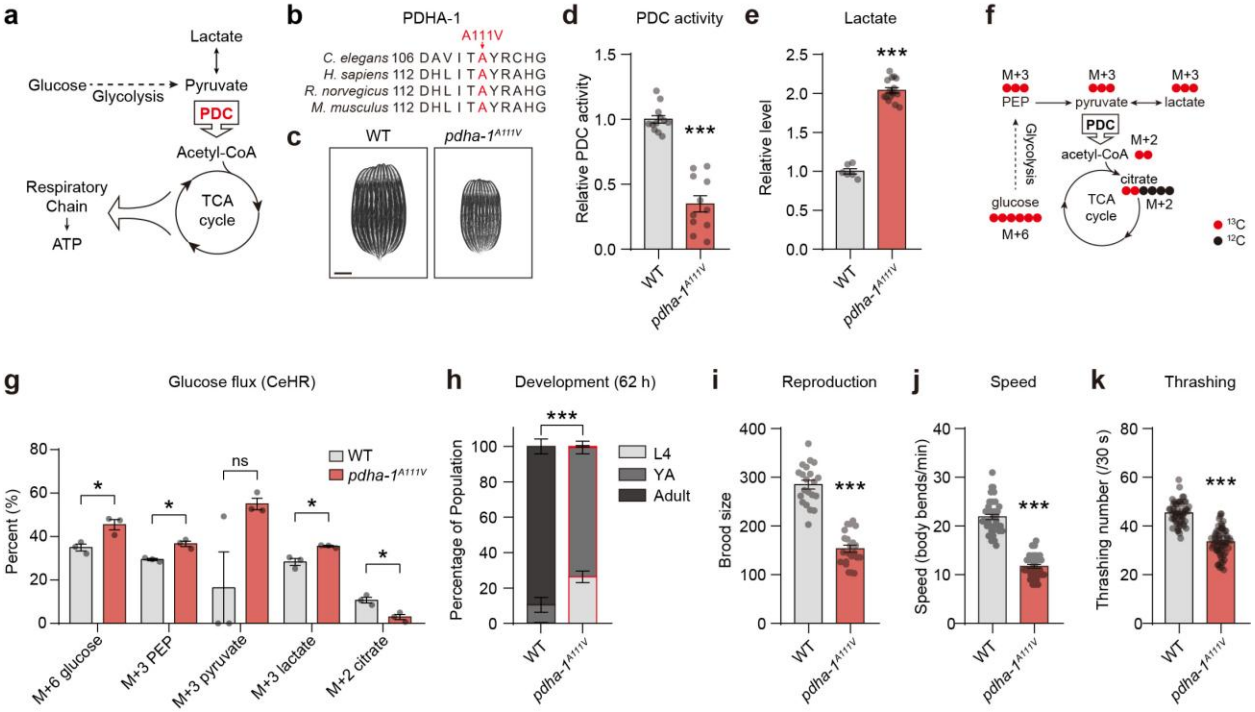

Figure 1. Establishment of a *C. elegans* model of PDCD.

(a) Schematic of PDC function in connecting glycolysis to mitochondrial metabolism.

(b) Cross-species alignment confirming conservation of the A111V mutation in PDHA-1.

(c) Representative images of WT and *pdha-1*^{A111V} mutant worms. Scale bar, 200 μm.

(d, e) Functional validation of the model: PDC enzymatic activity (d) and lactate levels (e) in WT and *pdha-1*^{A111V} mutants.

(f, g) Metabolic flux analysis using [U-$^{13}C_6$] glucose: tracing schematic (f) and isotopomer distributions(g).

(h-k) Phenotypic characterization of *pdha-1*^{A111V} mutants: Developmental timing assessed 62 hours after L1 larval plating (h), brood size (i), locomotion speed (j), and thrashing frequency (k). Data are mean ± SEM. $*p < 0.05$, $**p < 0.01$, $***p < 0.001$, ns, not significant; two-sided unpaired t test for (d), (e), and (i-k); two-way ANOVA for (g) and (h). N ≥ 3 biological replicates.

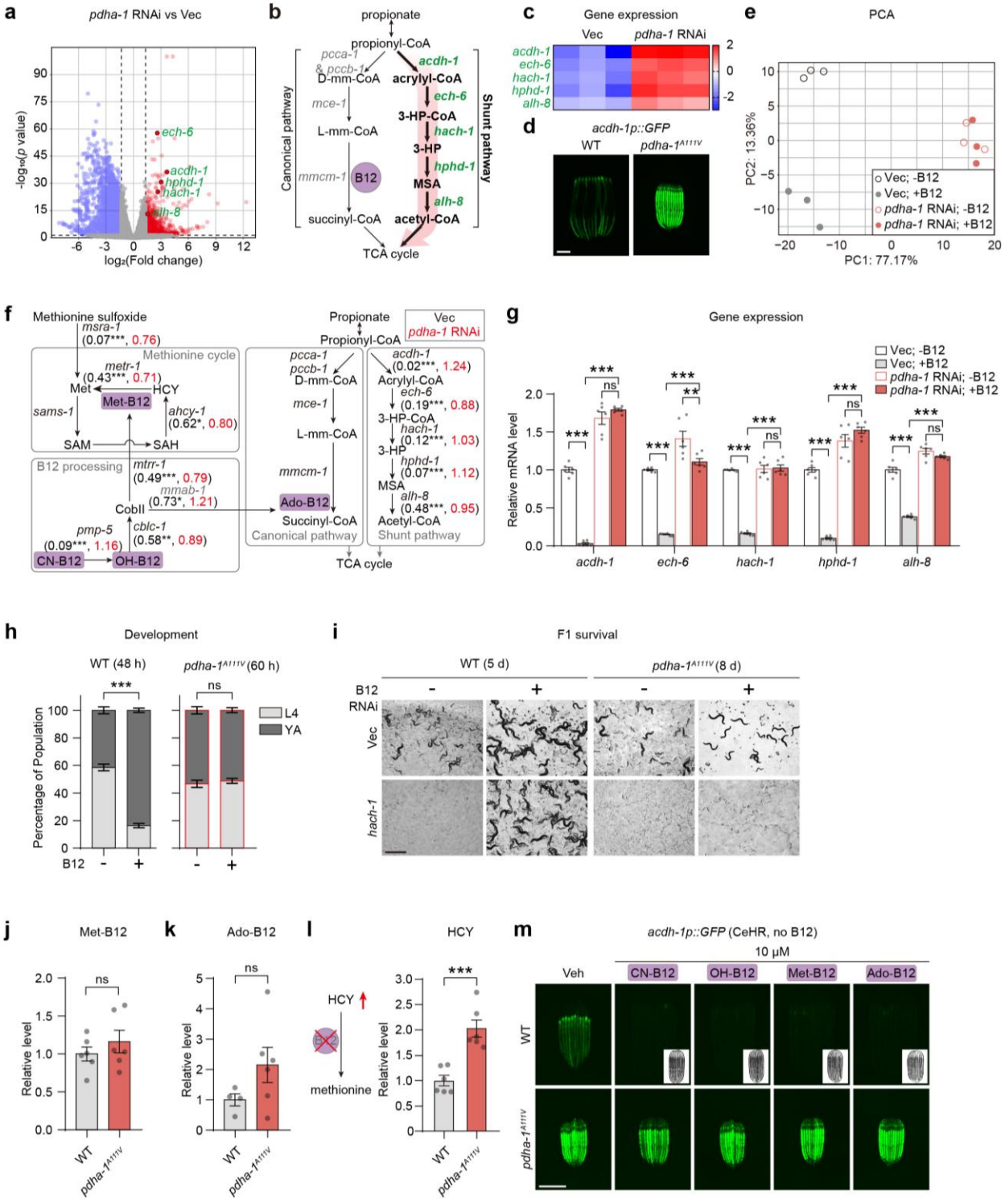

Figure 2. PDCD induces B12 dysfunction in *C. elegans*

(a) Volcano plots for the comparison of *pdha-1* RNAi versus vector control. Significantly up-regulated (fold change > 2, adjusted $p < 0.05$) and down-regulated (fold change < 0.5, adjusted p

865 < 0.05) genes are colored red and blue, respectively. Genes comprising the propionate shunt are
866 highlighted with green labels.
867 (b) Schematic of the propionate breakdown pathways. mm-CoA, methylmalonyl-CoA; 3-HP, 3-
868 hydroxypropionate; MSA, malonic semialdehyde.
869 (c) Heatmap showing expression of propionate shunt genes.
870 (d) Reporter expression of *acdh-1* reporter in WT and *pdha-1*^{A111V} mutant animals. Scale bar, 200
871 μm.
872 (e) Principal Component Analysis (PCA) of RNA-seq data from control or *pdha-1* RNAi worms
873 on B12-sufficient or B12-deficient diets.
874 (f) Schematic of B12 processing and utilization pathways. Genes significantly responsive to B12
875 are shown. Numbers denote the fold-change (B12+versus B12-) in control (black) and *pdha-1*
876 RNAi (red) groups. Numbers without makers represent non-significant changes.
877 (g) Relative mRNA levels of key genes in control vs. *pdha-1* RNAi, ±B12.
878 (h) Developmental stage distribution of WT and *pdha-1*^{A111V} mutants ± B12, assessed 48h (WT)
879 and 60 h (mutant) after L1 larval plating.
880 (i) Offspring survival outcome of WT and *pdha-1*^{A111V} mutants subjected to control or *hach-1*
881 RNAi, ±B12 supplementation.
882 (j, k) Relative levels of met-B12 (j) and ado-B12 (k) in WT and *pdha-1*^{A111V} mutants.
883 (l) *pdha-1*^{A111V} mutants accumulate HCY. Schematic of B12-dependent HCY metabolism (Left).
884 Relative HCY levels in WT and mutant animals (Right).
885 (m) Reporter induction in WT and *pdha-1*^{A111V} mutant animals treated with different forms of B12
886 in CeHR medium. Insets show DIC images. CN-B12, cyanocobalamin; OH-B12,
887 hydroxocobalamin; met-B12, methyl-cobalamin; ado-B12, adenosyl-cobalamin. Scale bar, 200
888 μm.

889 Data are mean ± SEM. ns, not significant, *$p < 0.05$, **$p < 0.01$, ***$p < 0.001$, ns, not significant;
890 two-sided unpaired t test for (f) and (j-l); two-way ANOVA for (g) and (h). N ≥ 3 biological
891 replicates.

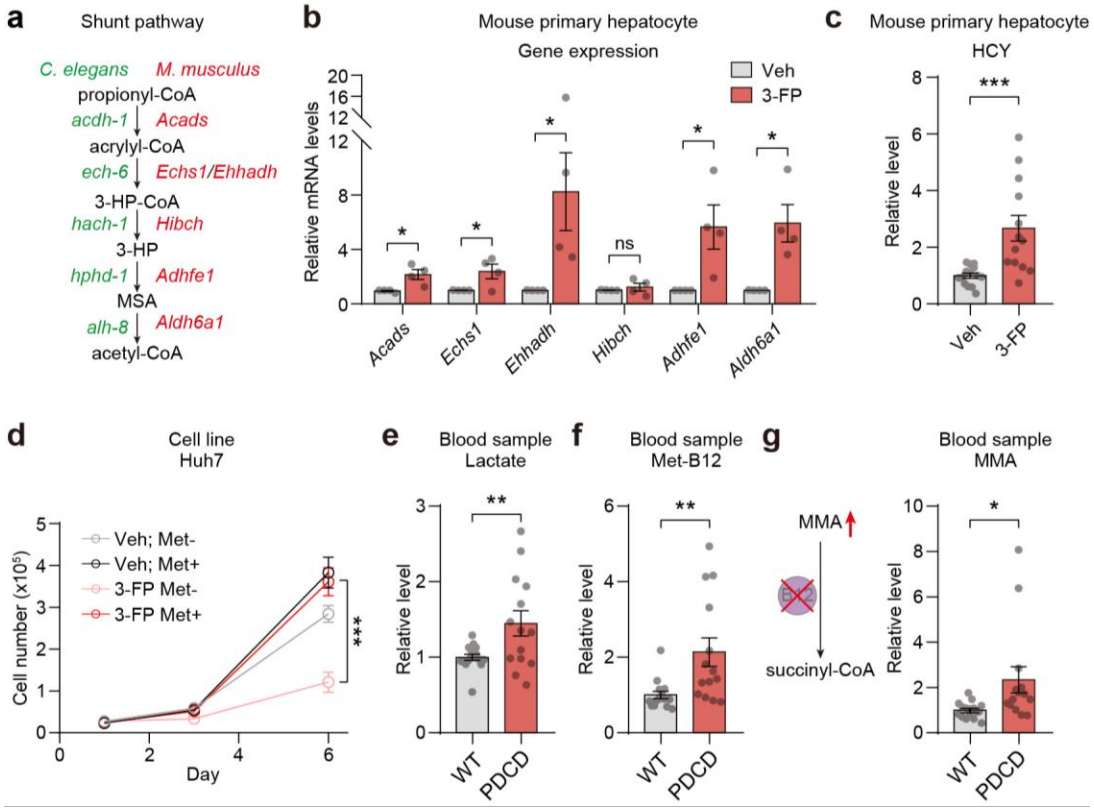

Figure 3. PDCD-induced B12 dysfunction is conserved in mammalian models and patients

(a) Comparative schematic of propionate shunt genes in *C. elegans* (green) and mouse (red).

(b, c) Treatment of mouse primary hepatocytes with the PDC inhibitor 3-fluoropyruvate (3-FP) increased mRNA levels of propionate shunt genes (b) and elevated HCY (c).

(d) 3-FP impaired Huh7 cell growth in a methionine-restricted (Met-) context.

(e-g) Metabolic profiling comparing PDCD patient samples to WT controls. Shown are the levels of lactate (e), methyl-B12 (f), and MMA(g). Schematic of B12-dependent MMA metabolism (g, left).

Data are mean ± SEM. ns, not significant, $*p < 0.05$, $**p < 0.01$, $***p < 0.001$, ns, not significant; two-sided unpaired t test for (b), (c), and (e-g); two-way ANOVA for (D). N ≥ 3 biological replicates.

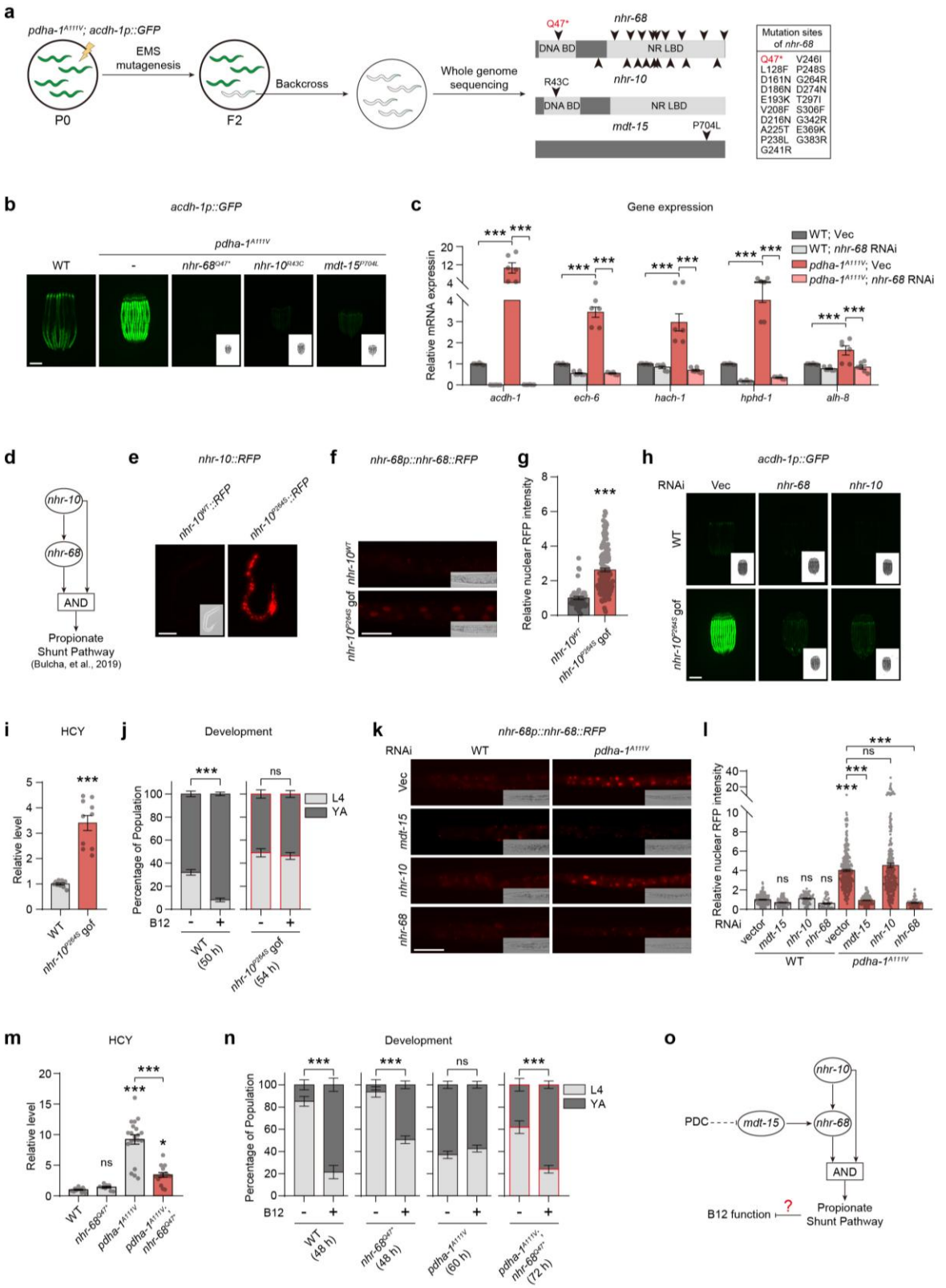

Figure 4. PDCD impairs B12 function via activation of the MDT-15-NHR-68-mediated shunt pathway.

(a) Forward genetic screen for suppressors of *acdh-1p::GFP* induction in *pdha-1*^{A111V} mutants. Arrowheads indicate identified mutation sites in indicated genes; corresponding mutation sites in *nhr-68* are listed in the right box.

(b) Representative images of the *acdh-1* reporter expression in the indicated genetic backgrounds. Insets show DIC images. Scale bar, 200 μm.

(c) Relative mRNA levels of the indicated genes in WT and *pdha-1*^{A111V} mutants subjected to control or *nhr-68* RNAi.

(d) Schematic of known regulatory interaction between NHR-10 and NHR-68[24].

(e) Representative images of the *nhr-10*^{WT}*::RFP* and *nhr-10*^{P264S}*::RFP* reporters at the L1 stage. Insets show DIC images. Scale bar, 50 μm.

(f, g) Representative images (f) and quantification (g) of NHR-68::RFP nuclear localization in the *nhr-10*^{WT} *and nhr-10*^{P264S} *gof* genetic backgrounds. *gof* gain-of-function. Scale bar, 50 μm.

(h) Representative images of the *acdh-1* reporter expression in WT and *nhr-10*^{P264S} *gof* animals subject to indicated RNAis. Insets show DIC images. Scale bar, 200 μm.

(i, j) The *nhr-10*^{P264S} *gof* mutants phenocopied PDCD by elevating HCY (i) and disrupting B12-dependent developmental acceleration (j).

(k, l) Representative images (k) and quantification (l) of NHR-68::RFP nuclear localization in *pdha-1*^{A111V} mutants, subject to control, *mdt-15*, *nhr-10*, or *nhr-68* RNAi. Insets show DIC images. Scale bar, 50 μm.

(m, n) The *nhr-68*^{Q47*} loss-of-function mutation suppressed HCY accumulation (m) and restored B12-mediated developmental effects (n) in *pdha-1*^{A111V} mutants, assessed at indicated conditions after L1 larval plating.

(o) Working model for PDC regulation of propionate shunt metabolism and B12 function.

Data are mean ± SEM. *$p < 0.05$, **$p < 0.01$, ***$p < 0.001$, ns, not significant; two-sided unpaired t test for (g) and (i); one-way ANOVA for (l) and (m); two-way ANOVA for (c), (j), and (n). N ≥ 3 biological replicates.

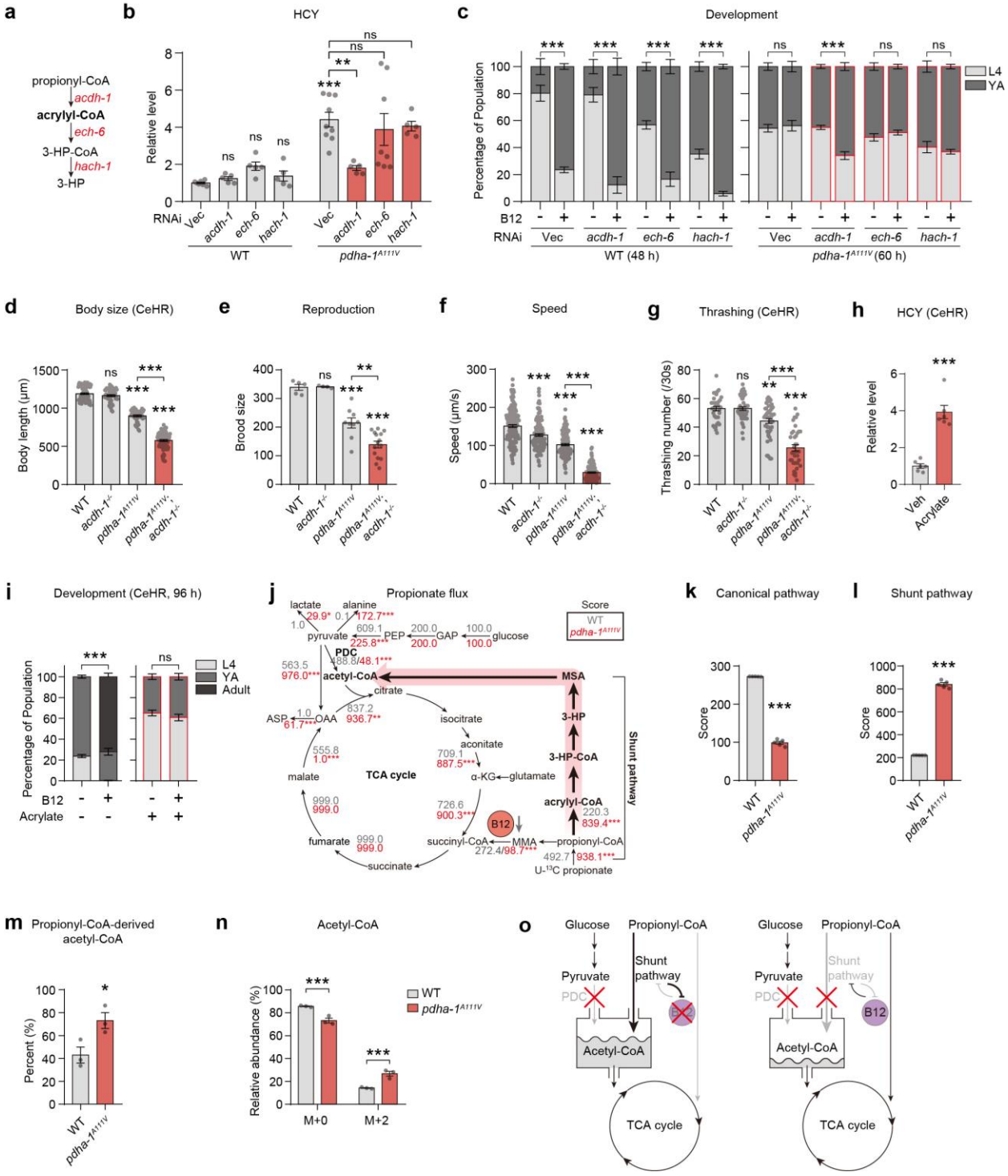

Figure 5. The propionate shunt fuels acetyl-CoA production while inducing B12 dysfunction in PDCD.

(a-c) Effects of RNAi targeting genes in the shunt pathway (a) on HCY levels (b) and developmental rates (c) in WT and *pdha-1*^{A111V} mutants ± B12 supplementation.

(d-g) Deletion of *acdh-1* exaggerated multiple physiological defects in *pdha-1*^{A111V} mutants, including reduced body size (d), brood size (e), locomotion speed (f), and thrashing frequency (g), under the indicated conditions.

(h, i) Acrylate supplementation phenocopied PDCD, increasing HCY (h) and impairing B12-depedent development (i) under the indicated conditions.

(j-l) Metabolic flux analysis using [U-$^{13}C_3$] propionate in WT and *pdha-1*^{A111V} mutants. Network model showing calculated metabolic activity (j); Activity changes for B12-dependent (canonical) (k) and B12-independent (shunt) (l) pathways.

(m, n) Increased acetyl-CoA derived from propionate in PDCD, as evidenced by the increased fraction of acetyl-CoA derived from propionyl-CoA(m) and higher absolute amount of ^{13}C-labeled acetyl-CoA (n) in *pdha-1*^{A111V} mutants compared to WT.

(o) Working model of propionate shunt-involved carbon rerouting and B12 dysfunction in PDCD.

Data are mean ± SEM. $*p < 0.05$, $**p < 0.01$, $***p < 0.001$, ns, not significant; two-sided unpaired t test for (h) and (k-m); one-way ANOVA for (d-g); two-way ANOVA for (b), (c), (i), and (n). N ≥ 3 biological replicates.

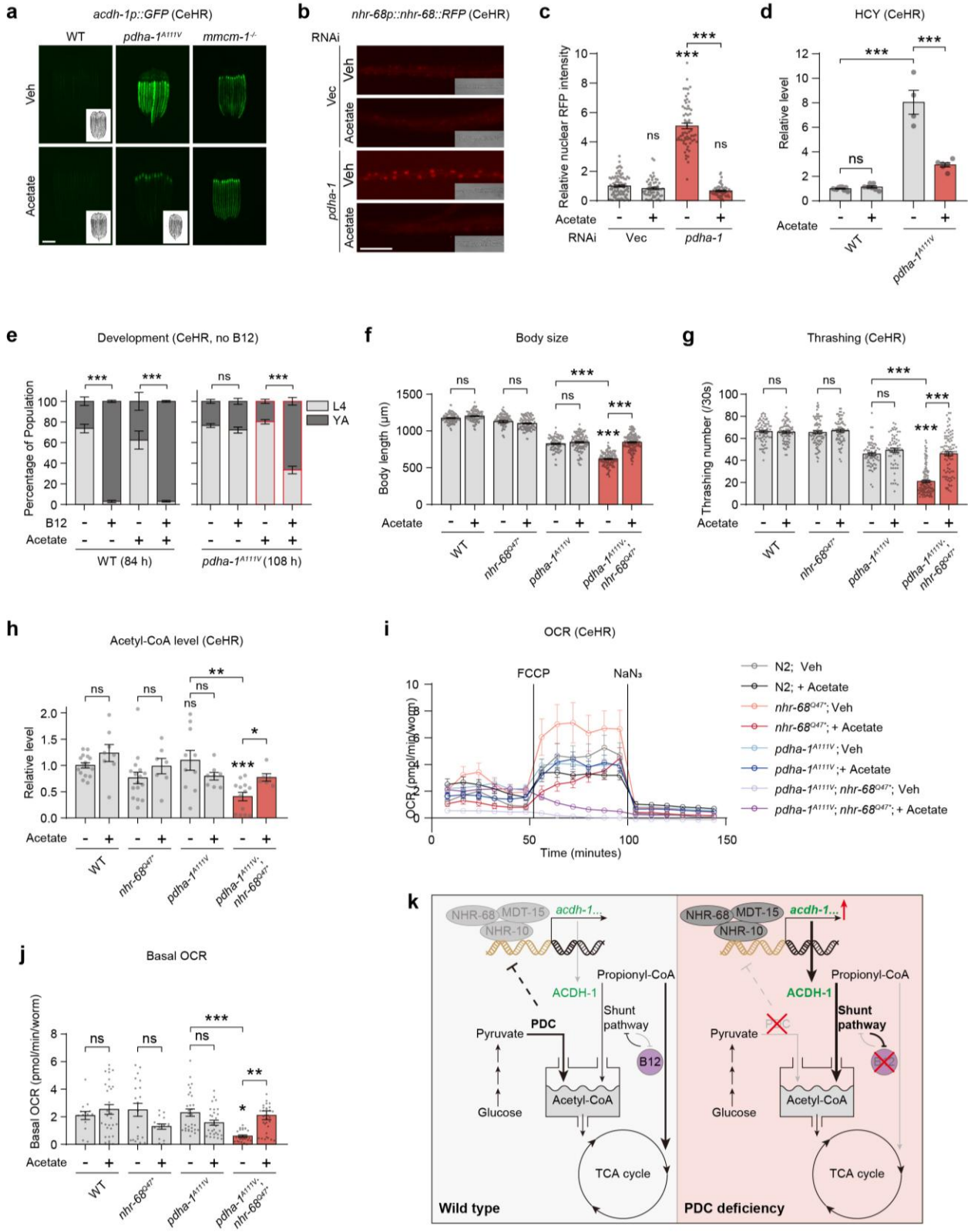

Fig 6. Acetate supplementation restores acetyl-CoA homeostasis and rescues B12 dysfunction in PDCD.

(a) Representative images of the *acdh-1* reporter in WT, *pdha-1*^{A111V} and *mmcm-1*$^{-/-}$ animals grown in CeHR medium supplemented with acetate. Insets show corresponding DIC images. Scale bar, 200 μm.

(b, c) Representative images (b) and quantification (c) of NHR-68::RFP expression in WT and *pdha-1*^{A111V} animals cultured in acetate-supplemented CeHR medium. Insets show corresponding DIC images. Scale bar, 50 μm.

(d-h) Metabolic and phenotypic analyses under the indicated genetic and culture conditions, including HCY levels (d), B12-dependent developmental progression (e), body size (f), thrashing rate (g), and acetyl-CoA levels (h).

(i, j) OCR dynamics (i) and basal OCR (j) in the indicated strains following acetate supplementation in CeHR medium.

(k) Proposed model illustrating PDCD-induced metabolic rewiring, which compromises B12 function as a trade-off.

Data are mean ± SEM. *$p < 0.05$, **$p < 0.01$, ***$p < 0.001$, ns, not significant; one-way ANOVA for (c); two-way ANOVA for (d-h) and (j). N ≥ 3 biological replicates.

Acknowledgments

We thank Drs. Kang Shen, Cen Xie, Cunqi Ye, Haojie Yu and Ben Zhou for their crucial discussions; We also thank Dr. Cunqi Ye and the Westlake Biomedical Research Core Facilities for providing technical assistance with metabolic flux analysis, and Drs. Fei-hong Luo, Shengying Qin, and Zhengxiao Fan for their assistance in seeking clinical resources. We acknowledge the *C. elegans* Genetics Center (P40 OD010440) for providing strains. During manuscript preparation, we utilized DeepSeek to enhance text readability and language. This study was supported by the National Natural Science Foundation of China 32271357 (L.W.) and 32200968 (D.D.), Zhejiang Provincial Natural Science Foundation of China under Grant LQ23C070002 (D.D.) and Westlake Education Foundation.

Author contributions

L.W. and D.D. conceived, designed, supervised and provided funding for this work and the writing of the paper. D.D., C.Q., J.C, and Z.L. carried out experiments and analysis. S.L. carried out the automated metabolic flux analysis. S.Z. optimized the CeHR. X.H., W.L., S.W., Z.W., T.Z., B.W., and H.D. aided in human blood sample collection. All authors provided critical feedback in writing the paper.

Competing interests

Authors declare that they have no competing interests.

Corresponding authors

994 Correspondence to wulianfeng@westlake.edu.cn (L.W.); 6305022@zju.edu.cn (X.H.);
995 wei_lu@fudan.edu.cn (W.L.); wushengnan@shchildren.com.cn (S.W.), or zhiyingwu@zju.edu.cn
996 (Z-Y.W.)

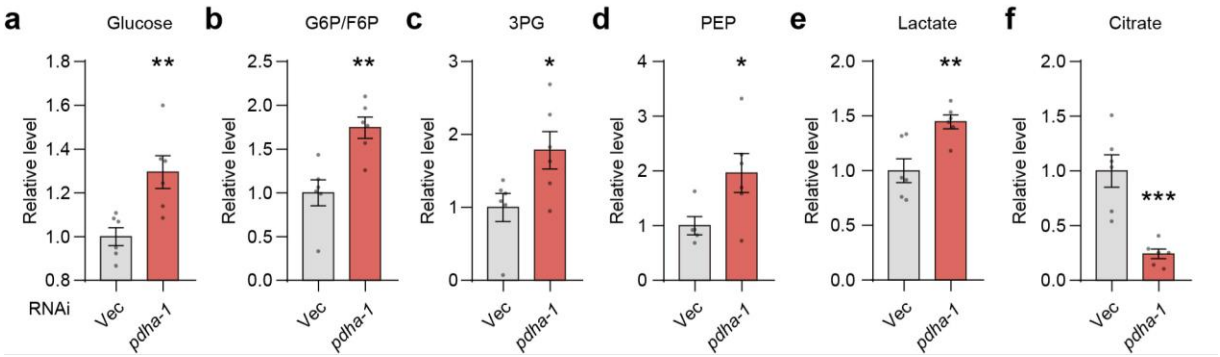

Extended Data Fig. 1. Knockdown of *pdha-1* increases glycolytic metabolites and reduces citrate.

(a-f) Relative levels of key metabolites in worms fed control or *pdha-1* RNAi.

Data are mean ± SEM. $*p < 0.05$, $**p < 0.01$, $***p < 0.001$, ns, not significant; two-sided unpaired *t* test. N ≥ 3 biological replicates.

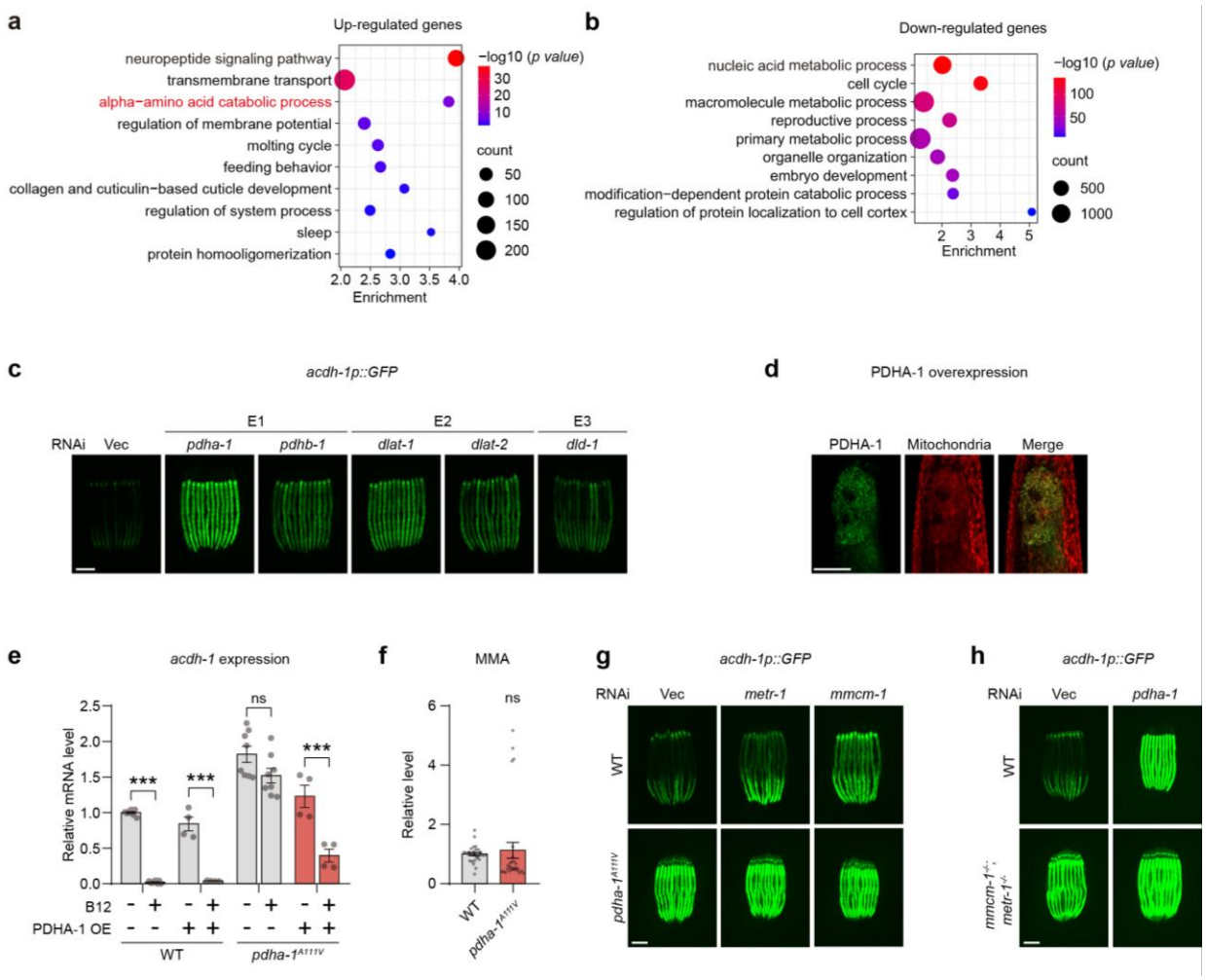

Extended Data Fig. 2. Supporting evidence for B12 dysfunction in PDCD worms.

(a and b) Gene ontology (GO) analysis of the upregulated (a) and downregulated (b) DEGs (FC > 2, $p < 0.05$) from *pdha-1* versus control RNAi-treated worms.

(c) Representative images of the *acdh-1* reporter induction by RNAi targeting multiple PDC subunit genes. Scale bar, 200 μm.

(d) Subcellular localization of PDHA-1::GFP in intestinal mitochondria, visualized by co-staining with CNB dye. Scale bar, 20 μm.

(e) Relative mRNA levels of *acdh-1* in WT and *pdha-1*^{A111V} mutants, ±B12, with or without intestine-specific PDHA-1 rescue.

(f) Relative levels of MMA in WT and *pdha-1*^{A111V} mutants.

(g) Representative images of the *acdh-1* reporter expression in WT and *pdha-1*^{A111V} mutants subjected to RNAi against vector, *metr-1*, or *mmcm-1*. Scale bar, 200 μm.

(h) Representative images of the *acdh-1* reporter in *mmcm-1*$^{-/-}$*; metr-1*$^{-/-}$ double mutant worms fed control or *pdha-1* RNAi. Scale bar, 200 μm.

Data are mean ± SEM. **p* < 0.05, ***p* < 0.01, ****p* < 0.001, ns, not significant; two-way ANOVA for (e); two-sided unpaired *t* test for (f). N ≥ 3 biological replicates.

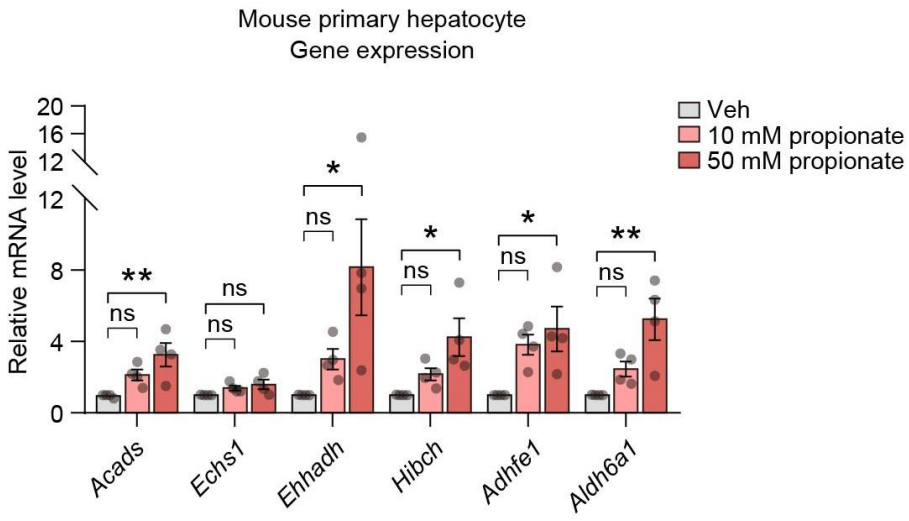

Extended Data Fig. 3. Propionate activates shunt gene expression in mouse primary hepatocytes.

Relative mRNA levels of the indicated genes in mouse primary hepatocytes treated with propionate.

Data are mean ± SEM. *$p < 0.05$, **$p < 0.01$, ***$p < 0.001$, ns, not significant; one-way ANOVA. N ≥ 3 biological replicates.

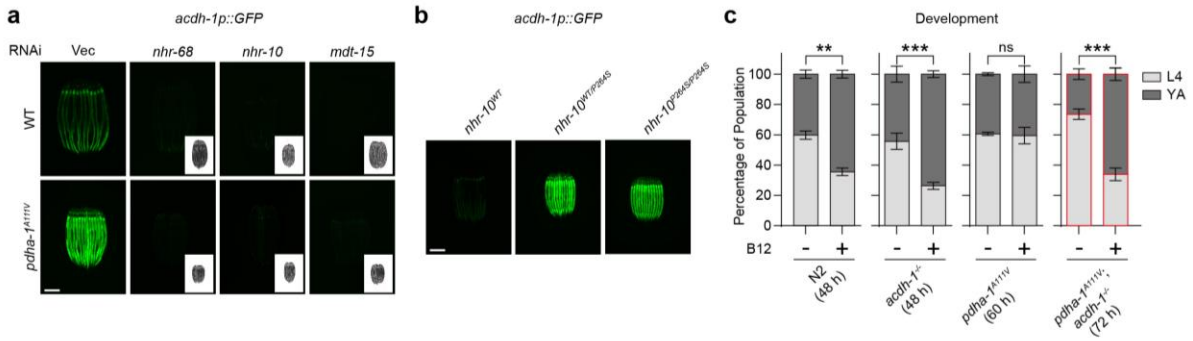

Extended Data Fig. 4. Supplementary genetic analysis of the PDCD-propionate shunt axis.

(a) Representative images of the *acdh-1* reporter in WT and *pdha-1*^{A111V} mutant animals treated with indicated RNAi. Insets show DIC images. Scale bar, 200 µm.

(b) Representative images of the *acdh-1* reporter in *nhr-10*^{WT}, *nhr-10*$^{WT/\ P264S}$ heterozygote, and *nhr-10*^{P264S} homozygote animals. Scale bar, 200 µm.

(c) Developmental stage distribution of WT, *acdh-1*$^{-/-}$, *pdha-1*^{A111V} mutants, and *pdha-1*^{A111V}*; acdh-1*$^{-/-}$ double mutants ±B12 supplementation, assessed at indicated time after L1 larval plating. Data are mean ± SEM. **p* < 0.05, ***p* < 0.01, ****p* < 0.001, ns, not significant; two-way ANOVA for (c). N ≥ 3 biological replicates.

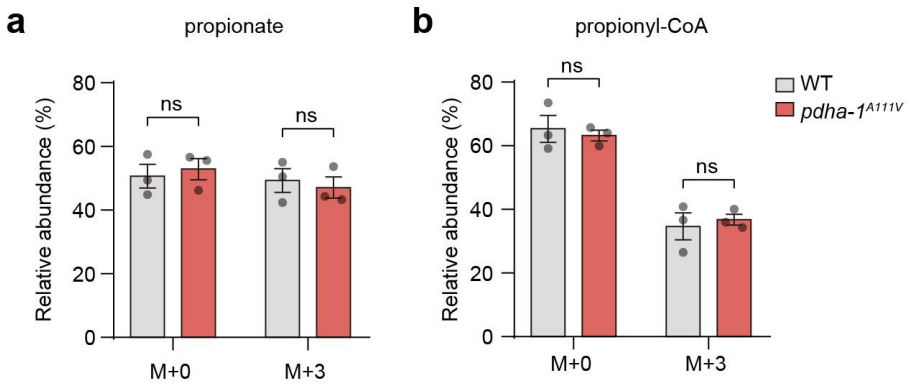

Extended Data Fig. 5. PDCD does not affect total propionate or propionyl-CoA abundance.

(a, b) Isotopic labeling patterns of (a) propionate and (b) propionyl-CoA measured following [U-$^{13}C_3$] propionate supplementation.

Data are mean ± SEM. $*p < 0.05$, $**p < 0.01$, $***p < 0.001$, ns, not significant; two-way ANOVA. N ≥ 3 biological replicates.

Supplementary Table 1. Human blood sample information

Source	Sample No.	Mutation gene	Mutation site	Zygosity	Age	Gender
Children's Hospital, Zhejiang University School of Medicine	Patient_1	*PDHA1*	c.836C>T	Heterozygote	7M17D	Female
	Patient_2	*PDHA1*	c.214C>G	Heterozygote	1Y10M	Female
	Patient_3	*PDHA1*	c.380G>T	Heterozygote	3Y6M	Female
	Patient_4	*PDHA1*	c.1159_1162dup	Hemizygote	6Y11M	Male
	Patient_5	*PDHB*	c.377del；c.430T>C	Heterozygote	9M6D	Female
	Control_1	-	-	-	4Y1M	Female
	Control_2	-	-	-	3Y8M	Female
	Control_3	-	-	-	2Y	Female
	Control_4	-	-	-	3Y2M	Female
	Control_5	-	-	-	5M5D	Male
	Control_6	-	-	-	2Y5M	Male
	Control_7	-	-	-	3Y11M	Male
	Control_8	-	-	-	2Y4M	Male
Second Affiliated Hospital, Zhejiang University School of Medicine	Patient_6	*PDHA1*	c.1159_1162dupAAGT	Hemizygote	6Y	Male
	Patient_7	*PDHA1*	c.1141A>T	Hemizygote	13Y	Male
	Control_9	-	-	-	52Y	Male
	Control_10	-	-	-	31Y	Female
Shanghai Children's Hospital, School of Medicine, Shanghai Jiao Tong University	Patient_8	*PDHA1*	c.1132C>G	Heterozygote	8Y	Female
	Patient_9	*PDHA1*	c.613T>G	Heterozygote	1Y7M	Female
	Control_11	-	-	-	6Y	Female
	Control_12	-	-	-	12Y	Male
	Patient_10	*PDHA1*	c.730_733del	Heterozygote	1Y7M	Female

Children's Hospital of Fudan University	Patient_11	*PDHA1*	c.1159_1162dupAAGT	Hemizygote	3Y0M	Male
	Patient_12	*PDHA1*	c.379C>T	Hemizygote	1M14D	Male
	Patient_13	*PDHA1*	c.214C>T	Hemizygote	3Y4M	Male
	Patient_14	*PDHA1*	c.1162del	Hemizygote	1Y9M	Male
	Control_13	-	-	-	1Y7M	Female
	Control_14	-	-	-	3Y1M	Male
	Control_15	-	-	-	3Y4M	Male
	Control_16	-	-	-	1Y9M	Male

1051